# Smart City Application 2019

Viser Technology Pte.Ltd. www.viserdata.com ISSN:2630-5305

Volume 2 No.5

Special Issue for 2019 World Transport Convention

VISER

# COMPANY INTRODUCTION

# 公司简介

维泽科技文化有限公司(Viser Technology Pte. Ltd. )成立于新加坡，是一家科技与文化高度融合的创新型企业。我们拥有一支具有较高文化素质、管理素质和业务素质的团队，聚焦于国际开源中英文期刊、体现文化含量与学术价值图书的出版发行。秉承“传播科技文化，促进学术交流”的理念，与国内外知名院校，科研院所及数据库建立了稳定的合作关系。坚持开拓创新，实施“跨越–融合”的发展战略，立足中国、新加坡两地，辐射全球，并于中国设立河北和重庆两个分部。我们将紧紧围绕专业化、特色化的发展道路，不断营造“有情怀，有视野，有梦想”的企业文化氛围，独树一帜，做一家“有血、有肉、有温度”的创新型出版企业。

Viser Technology Pte. Ltd. was founded in Singapore with branch offices in both Hebei and Chongqing, China. Viser focuses on publishing scientific and technological journals and books that promote the exchange of scientific and technological findings among the research community and around the globe. Despite being a young company, Viser is actively connecting with well-known universities, research institutes, and indexation database, and has already established a stable collaborative relationship with them. We also have a group of experienced editors and publishing experts who are dedicated to publishing high-quality journal and book contents. We offer the scholars various academic journals covering a variety of subjects and we are committed to reducing the hassles of scholarly publishing. To achieve this goal, we provide scholars with an all-in-one platform that offers solutions to every publishing process that a scholar needs to go through in order to show their latest finding to the world.

# Smart City Application

Special Issue for 2019 World Transport Convention

**Publisher:** Viser Technology Pte. Ltd.
**ISSN:** 2630-5305
**Frequency:**Monthly
**Add.:**21 Woodlands Close, #08-18,
Primz Bizhub SINGAPORE (737854)
**https://www.viserdata.com/**

VISER

*Smart City Application*

Volume 2 No. 5 (2019)

# CONTENTS

# A Deep Reinforcement Learning Based Car Following Model for Electric Vehicle

**Yuankai Wu[1], Huachun Tan[2], Jiankun Peng[3], Bin Ran[4]**

1 School of Mechanical Engineering, Beijing Institute of Technology, No 5 yard, South Zhongguanchun Road, Beijing, China
2 School of Transportation Engineering, Southeast University, Sipailou 2, Nanjing, Jiangsu, China
3 School of Mechanical Engineering, Beijing Institute of Technology, No 5 yard, South Zhongguanchun Road, Beijing, China
4 Department of Civil and Environmental Engineering, University of Wisconsin-Madison,1415 Engineering Drive, Madison, WI, USA

## Abstract

Car following (CF) models are an appealing research area because they fundamentally describe longitudinal interactions of vehicles on the road, and contribute significantly to an understanding of traffic flow. There is an emerging trend to use data-driven method to build CF models. One challenge to the data-driven CF models is their capability to achieve optimal longitudinal driven behavior because a lot of bad driving behaviors will be learnt from human drivers by the supervised learning manner. In this study, by utilizing the deep reinforcement learning (DRL) techniques trust region policy optimization (TRPO), a DRL based CF model for electric vehicle (EV) is built. The proposed CF model can learn optimal driving behavior by itself in simulation. The experiments on following standard driving cycle show that the DRL model outperforms the traditional CF model in terms of electricity consumption.

**Keywords:** *autonomous electric vehicle, car following model, deep reinforcement learning, trust region policy optimization*

## 1. Introduction

Electric vehicle (EV) and autonomous vehicle (AV) are two flourishing technologies which would promote environment sustainability and improve community livability. Accomplish of the high level autonomous electric vehicle (AEV) requires breakthrough in numerous technology, among which longitudinal dynamics control is an unquestionable key factor gearing up the safety and efficiency of AEV.

In the transportation research field, car-following models have been successfully applied to describe longitudinal driving behavior under car following (CF) scenario. In order to analyze traffic flow in simulation program as simple as possible, researchers are often interested in describing CF behavior with mathematical models (Chandler et.al 1958, Maerivoet & De Moor, 2005). Although mathematical model based CF models are powerful and useful tools for analysis of driving behavior, there still require significant improvements. First, a calibration process is required for most models before they are able to analyze and simulate real traffic dynamics. Calibration, however, is a onerous process needed further studies (Punzo et.al, 2012). Second, the dynamics between driving environment and CF decision is very complex. A simple mathematical model is not able to fully model the correlation between environment and decision.

Recent developments in the field of big data have led to an interest in development of data-driven CF models (He et.al, 2015). Neural networks (NNs), a learning system with universal approximation ability, have been extensively used to describe CF behaviors because their ability to imitate human learning process from data. For example, Chong et.al, (2013) attempts to use fuzzy NNs to achieve data-driving CF models. Hongfei et.al, (2003) shows that the NNs models could accurately describe the following behavior of a driver after the training course on field data. Several studies (Khodayari et.al, 2012, Zheng et.al, 2013) have incorporated reaction delay into NNs models.

In recent years, deep learning (NNs with deep structure) have won numerous contests in pattern recognition and machine learning (Schmidhuber, 2015). To better model the CF behavior, researches have been using deep learning technique. The deep recurrent neural networks (RNNs) are the most popular deep learning structure for model CF because of its capability to model memory effect in processing sequential data. Wang et.al, (2018) have recently developed a deep RNN model for the representation of memory effect in the CF model, it is reported that their model achieves higher prediction accuracy than shallow NNs based models. Similar researches can be found in (Zhou et.al, 2017, Huang et.al, 2018).

The above studies especially the deep learning approaches demonstrate great flexibility of neural networks for modeling

CF behavior. However, these neural networks are trained in a supervised learning manner using real drivers' trajectories. Create a datasets with perfect CF trajectories might be expensive and unfeasible. The human driver itself is not perfect, whose driving behavior is limited by reaction delay, bad temper and so on. Therefore a CF model trained by supervised learning has inevitably learned a lot of bad driving behaviors from imperfect drivers, therefore is difficult to provide the best CF behavior. In problems such as Go (Silver et.al, 2016) and computer games (Mnih et.al, 2015), reinforcement learning (RL) successfully address these challenges. The essence of RL is learning through interaction. RL agent interacts with its environment and, upon observing the consequences of its actions, can learn to alter its own behaviour in response to rewards received (Arulkumaran et.al, 2017). A RL agent can theoretically achieve behavior that maximizes cumulative reward.

Deep learning has greatly enhance RL, with the exploitation of deep learning algorithms within RL defining the field of“deep reinforcement learning” (DRL). There are numerous DRL approaches including deep Q networks (DQN) (Mnih et.al, 2015), Evolutionary Strategy (ES) (Salimans et.al, 2017) and various policy gradient methods, such as TRPO (Schulman et.al, 2015), A3C (Mnih et.al, 2016), DDPG (Lillicrap et.al, 2015) and PPO (Schulman et.al, 2017). Those algorithms hold great promise for learning to solve challenging decision make problems such as CF.

The goal of this paper is to utilize DRL to achieve economic and safe longitudinal driving for AEV. First, we build a simulation model for electric vehicle using real-world data. Then we formulate the CF model as a markovian decision process (MDP) and propose to use DRL algorithm to solve the MDP. Finally we conduct simulated experiments on the new european driving cycle (NEDC), the results show that the DRL based CF approach is more energy-efficient than conventional CF models.

## 2. The Simulation Model For Electric vehicle

The EV powertrain and appearance of Roewe E50 are shown in Figure 1. The powertrain is composed of a drive motor and a power battery. The efficiency map of the traction motor is given in Figure 2. The main parameters of Roewe E50 are listed in Table 1.

**Figure 1** The appearance and powertrain of Roewe E50

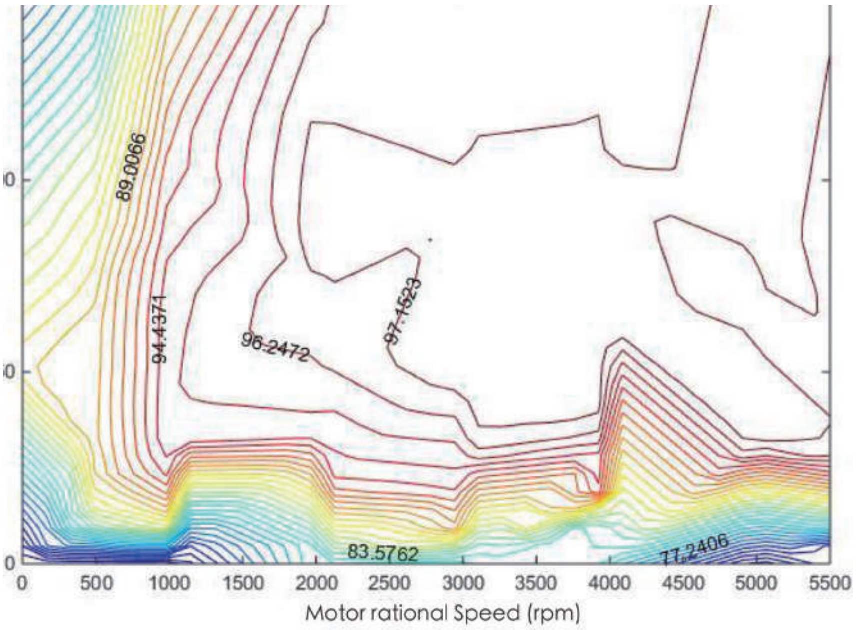

**Figure 2** The efficiency map of traction motor for Roewe E50

**Table 1** Main parameters of Roewe E50 specification

| Parameters | Value | Parameters | Value |
|---|---|---|---|
| Full mass | 1391.2kg | Air drag coefficient | 0.34 |
| Windward area | 1.83m$^2$ | Main reducer ratio | 6.2 |
| Rolling resistance coefficient | 0.0011 | Battery capacity | 77.7 Ah |
| Wheel radius | 0.262m | Peak velocity | 130 km/h |

There are two approaches to simulate the powertrain: the backward and forward approaches (Onori et.al, 2016). The backward approach is chosen in this paper. In a backward simulator, no driver model is necessary, the desired speed is a direct input to the simulator, and the energy consumption is output. The tractive force of the vehicle is calculated by:

$$F_{tr} = \delta ma + F_g + F_r + F_{AD}. \tag{1}$$

where $\delta$ is the rotational inertia coefficient, α is the acceleration of the vehicle, $F_g = mgsin\theta$,$F_r$ is the rolling resistance force $F_r = mgcos\theta C_r$, $C_r$ is the rolling resistance coefficient. $F_{AD} = 0.5p_aC_{AD}A_fv^2$, $p_a$ is the air density, $C_{AD}$ is the air drag coefficient, $A_f$ is the windward area, $v$ is the velocity of the vehicle.

The torque, rational speed and power of vehicle demand is computed by

$$T_{wh} = F_{tr}r_{wh},\ W_{wh} = \frac{v}{r_{wh}}, P_{wh} = T_{wh}W_{wh}. \tag{2}$$

where $r_{wh}$ is the Wheel radius. The power of the motor is $P_{mot} = P_{wh}/\eta_d$. $\eta_d$ is the transmission efficiency. The power of the battery is then computed by $P = P_{mot}/\eta_{mot}\cdot \eta_{mot}$. $\eta_{mot}$ is the efficiency of the motor, which is computed by the efficiency map given in Figure 2.

Then the battery current can be computed by

$$I = \frac{V_{oc} - \sqrt{V_{oc}{}^2 - 4RP}}{2R}. \tag{3}$$

$V_{oc}$ is the open-circuit voltage of the battery, and $R$ is the internal resistance of battery. Then the consume of SOC of the battery can be computed by

$$\Delta SOC = \frac{It}{Q}. \tag{4}$$

where Q is the battery capacity. To make sure the simulation model for EV is accurate, we compare the battery current of simulation model and real vehicle using a real trajectory. The result is given in Figure 3. The results show that the battery current curve of simulation model is close to the one of real vehicle.

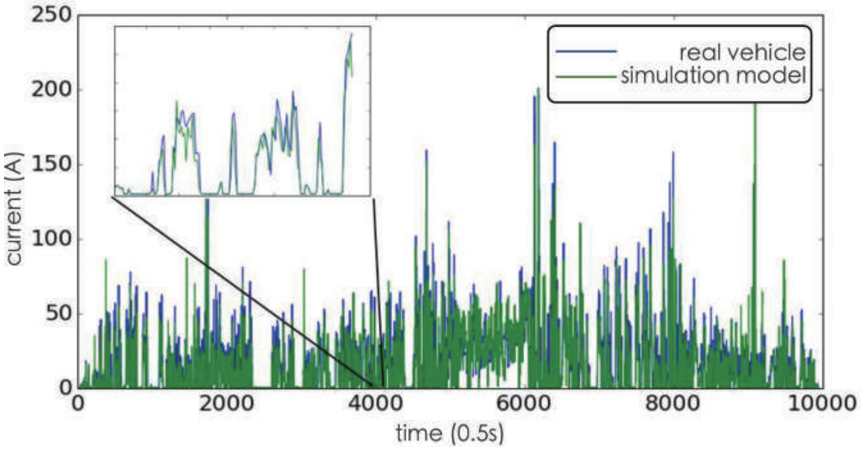

**Figure 3** The comparison between battery current of real vehicle and simulation model

## 3. Car Following As a markovian Decision Process

In this paper, we consider the problem of CF trajectory planning for AEV. The goal of the planning is to minimize the electricity consumption and simultaneously guarantee the safety and effectiveness of CF. Driving speed and gap of the leader are collected real-time by V2V devices and/or sensors of following vehicle. An illustration of the problem is available in Figure 4. The aim of CF trajectory planning is to decide the real-time acceleration of the follower.

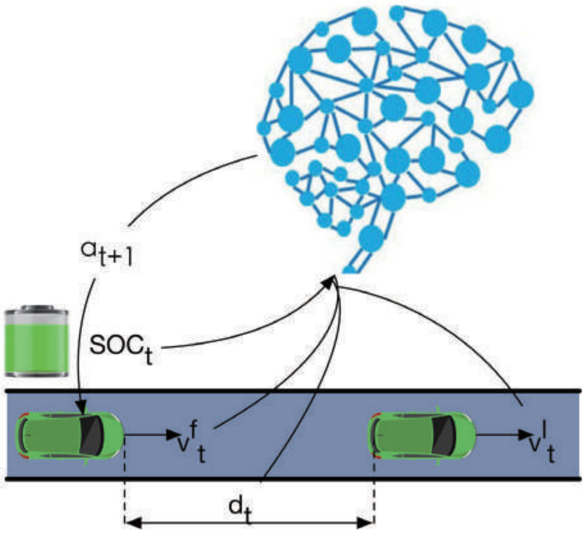

**Figure 4** The CF problem in this paper

To tackle this problem, we propose to formulate the problem using markovian decision process (MDP), which is defined as $\mathfrak{G} = (S, A, P, R, \gamma)$, where $S, A, P, R, \gamma$ are the sets of states, action space, transition probability functions, reward functions, and a discount factor respectively. The definitions are given as follows:

State $s_t \in S$: The state of the CF problem is defined as a vector:

$$s_t = \left(SOC_t, d_t, {v^l}_t, {v^f}_t\right). \tag{5}$$

where $SOC_t$ is the state of charge of follower's battery at time $t$, $d_t, {v^l}_t, {v^f}_t$ are the distance, speed of the leader, and speed of the follower at time $t$. The reason we choose $SOC_t$ as a state variable is that the electricity consumption is impacted by the $SOC$ of the battery.

Action $a_t \in A$: The action of the following vehicle is defined as its action. The acceleration is ranging from -3 to 3.

Reward function $r_t \in R = S \times A \rightarrow \mathcal{R}$: Since the follower should follow with the leader with an appropriate distance while save the electricity consumption, both the distance and electricity consumption should be taken into account in modelling reward. The reward is defined as the sum cost of the distance reward and electricity consumption as follows:

$$r_t = f_r\left(d_t, {v^f}_t\right) - Q\Delta SOC_t Price_e \tag{6}$$

where $f_r()$ is a function that mapping $d_t, {v^f}_t$ into the distance reward. $Price_e$ is the RMB cost for electricity. $f_r()$ is defined as:

$$f_r\left(d_t, {v^f}_t\right) = \begin{cases} -0.0035\left(0.1{v^f}_t - d_t\right), \ if\ 0.1 < d_t < 0.1{v^f}_t \\ -0.00175\left(d_t - {v^f}_t\right) \quad if\ d_t > {v^f}_t \\ -1 \quad if\ d_t \le 0.1 \end{cases}. \tag{7}$$

The distance reward function given in Eq (7) means that when the distance between leader and follower is below the safety distance the function outputs a low reward value. Moreover, the function also outputs a low reward value if the follower are too far away from the leader.

State transition probability $p(s_{t+1}|s_t, a_t)$: $S \times A \times S \rightarrow [0:1]$: It gives the probability of transiting to $s_{t+1}$ given a action $a_t$ is taken in the current state $s_t$. The transition of $SOC_t$ in Eq (5) is determined by the EV simulation model given in section 2. ${v^f}_t$ of state in Eq (5) is computed by ${v^f}_{t+1} = {v^f}_t + a_t$. $d_t$ and ${v^l}_t$ are determined by the future driving behaviour of the leader.

## 4. Trust Region Policy Optimization

The essence of DRL is to use deep learning techniques to search an optimal action policy for MDP. In this paper, we use a specific policy gradient method — Trust Region Policy Optimization (TRPO) to obtain CF policies. We introduce the basic principle of TRPO in this section.

In RL, we optimize a policy $\pi_\theta$ for the maximum expected discounted rewards:

$$\max_{\theta} J(\pi_\theta) = E_{r\sim\pi_\theta}(\textstyle\sum_{t=0}^{\infty}\gamma^t r_t). \tag{8}$$

The policy gradient (PG) computes the steepest ascent direction for the rewards and update the policy towards that direction.

$$g = \nabla_\theta J(\pi_\theta), \quad \theta_{k+1} = \theta_k + \alpha g. \tag{9}$$

A problem with PG is that improper learning rate $\alpha$ will cause vanishing or exploding gradient. Moreover, $J(\pi_\theta)$ is sensitive to noise or function approximation error. In order to make the optimization more robust, an advantage function is defined:

$$\begin{aligned} &Q_\pi(s_t,a_t) = E_{s_{t+1},a_{t+1},\dots}(\textstyle\sum_{t=0}^{\infty}\gamma^l r_{t+l}), \ \ V_\pi(s_t) = E_{a_t,s_{t+1},\dots}(\textstyle\sum_{t=0}^{\infty}\gamma^l r_{t+l}), \\ &A_\pi(s,a) = Q_\pi(s,a) - V_\pi(s). \end{aligned} \tag{10}$$

The advantage function $A_\pi()$ describes how good the action $a$ is compared to the average of all the action. Using the advantage function, the loss function of policy gradient becomes

$$\max_{\theta} J(\pi_\theta) = E_t(\log \pi_\theta(a_t|s_t)A_t). \tag{11}$$

In order to solve the problem using Monte Carlo simulation, the importance sampling method is applied to transform the loss function into the following form:

$$\max_{\theta^{old}} J(\pi_\theta) = E_t\left(\log \frac{\pi_\theta(a_t|s_t)}{\pi_{\theta old}(a_t|s_t)} A_t\right) \tag{12}$$

It is suggested that by maximize the following loss function, we are guaranteed to improve the policy:

$$\max_{\theta^{old}} \ E_t\left(\log \frac{\pi_\theta(a_t|s_t)}{\pi_{\theta old}(a_t|s_t)} A_t\right) - \beta E_t[KL[\pi_\theta(\cdot\,|s_t), \pi_{\theta^{old}}(\cdot\,|s_t)]] \tag{13}$$

where $KL(\cdot,\cdot)$ is KL divergence. The detail about the mathematical derivation of TRPO can be found in (Schulman et.al, 2015).

TRPO can be implemented via Actor-Crtic architecture, the advantage value $A_t$ can be estimated by the critic when training actor's parameters $\theta$. Both actor and critic can be parameterized by neural networks using parameters $\epsilon$ and $\theta$. The critic parameters $\epsilon$ is learnt using the gradients from the TD error signal:

$$\min_{\epsilon}(r_t + \gamma V^\epsilon(s_{t+1}) - V^\epsilon(s_t))^2 \tag{14}$$

The advantage function $A_t$ is estimated by $V^\epsilon(s_t) - (r_t + \gamma V^\epsilon(s_{t+1}))$. The algorithm for TRPO based CF is summarized in Algorithm 1.

Algorithm 1 Framework of TRPO for CF

```
Randomly initialize critic and actor network with parameters $\epsilon$ and $\theta$;
For episode = 1 to m do
    Receive initial observation state $s_0 = (SOC_0, d_0, v^l{}_0, v^f{}_0)$;
    For t = 1 to time length of following T do
        Select action $a_t$ according to the current actor;
        Execute action $a_t$ and observe reward $r_t$, new state $s_{t+1}$ using simulation EV model;
        Update actor parameters $\theta$ by maximizing the loss in (13);
        Update critic parameters $\epsilon$ by minimizing the loss in (14);
    end for
end for
```

## 5. Experimental Results

In this section, we present the quantitative and qualitative experiment results on following a vehicle driving with standard cycle NEDC. Their initial distance is 2m. The actor and the critic of the agent are composed of neural networks. Specifically, the actor $f^\theta()$ is expressed by:

$$h^a = relu(W_h{}^a s + b_h{}^a), a^\mu = 3\tanh\left(W_\mu h^a + b_\mu\right), a^\sigma = \mathrm{softplus}(W_\sigma h^a + b_\sigma) \tag{15}$$

where relu, tanh and softplus are nonlinear activations. $W_h{}^a \in R^{200\times 4}$ and $b_h{}^a \in R^{200\times 1}$ are the parameters for hidden layers of actor. $W_\mu \in R^{1\times 200}$ and $b_\mu \in R^{1\times 1}$ are the parameters for mean value of action. $W_\sigma \in R^{1\times 200}$ and $b_\sigma \in R^{1\times 1}$ are the parameters for variance of action. The acceleration of the vehicle is sampled from Gaussian distribution $N(\mu, \sigma^2)$. The critic $f^{\epsilon}()$ is expressed by:

$$h^c = relu({W_h}^c s + {b_h}^c), v = linear(W_v h^c + b_v) \tag{16}$$

where relu and linear are nonlinear activations. ${W_h}^c \in R^{200\times1}$ and ${b_h}^c \in R^{200\times1}$ are the parameters for hidden layers of critic. $W_v \in R^{1\times200}$ and $b_v \in R^{1\times1}$ are the parameters for value function estimation of critic. The actor and critic are built upon Tensorflow (https://www.tensorflow.org/).

The learning process of TRPO on CF is given in Figure 5. The agent achieves progressively high reward. It is observed that the agent is learnt to drive far behind the leader at the beginning because the electricity cost is very low if the vehicle drives very slow. Then the distance reward $f_r(d_t, {v^f}_t)$ motivates the agent to drive behind the leader closely, the average distance goes down and the RMB cost of electricity plateau at 1.3 ￥.

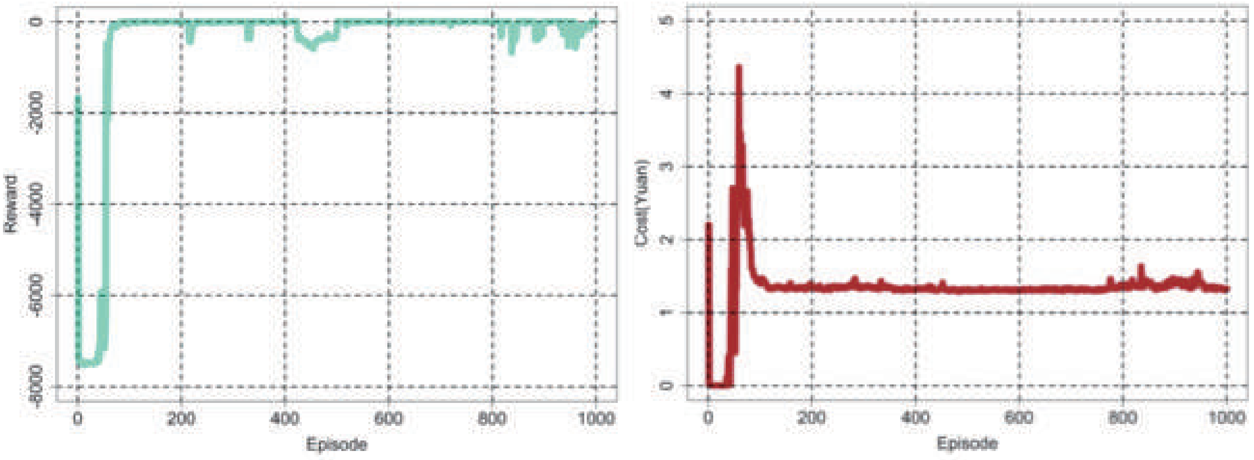

(a) The reward curve (b) The RMB cost curve

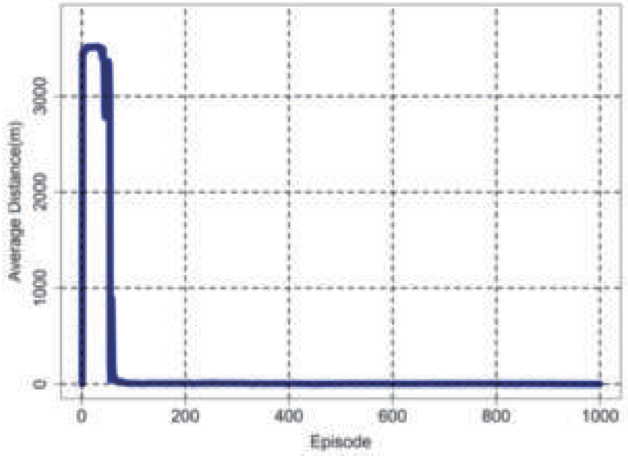

(c) The average distance curve

**Figure 5** The learning process of TRPO on CF

We compare the TRPO based CF model with several conventional CF models including Krauß, SmartSK, and Wiedemann models. Those models are well built-in SUMO- an open source traffic simulation software. The software is highly flexible, well documented and supports set the speed limits for each lane using its API--the Traffic Control Interface (TraCI) package. In SUMO, we set the leader driving with the speed from NEDC driving cycle, and the followers with different car following models are driving behind the leader. The initial distance between leader and follower is set to 2m. The minimum gap between leader and follower is set to 0.1m. The initial SOC of the simulated Roewe E50 is set to 0.85. The final SOC and RMB cost of the electricity consumption of different models are given in Table 2. It is obvious that the DRL based TRPO model outperforms other conventional CF models. The reason is that the DRL based CF model utilizes neural networks to model the CF behaviour, which has more powerful capability than model with simple mathematical equation. Moreover, the DRL based CF is trained by a reward-driven manner, thus can achieve optimal electricity consumption and following distance using the reward signal given in Eq (6).

**Table 2** The final SOC and RMB cost of different CF models

| Method | Final_SOC | RMB cost |
|---|---|---|
| TRPO | 0.7972 | 1.3261 |
| Krauss | 0.7833 | 1.6746 |
| SmartSK | 0.7210 | 3.2341 |
| Wiedemann | 0.7892 | 1.5296 |

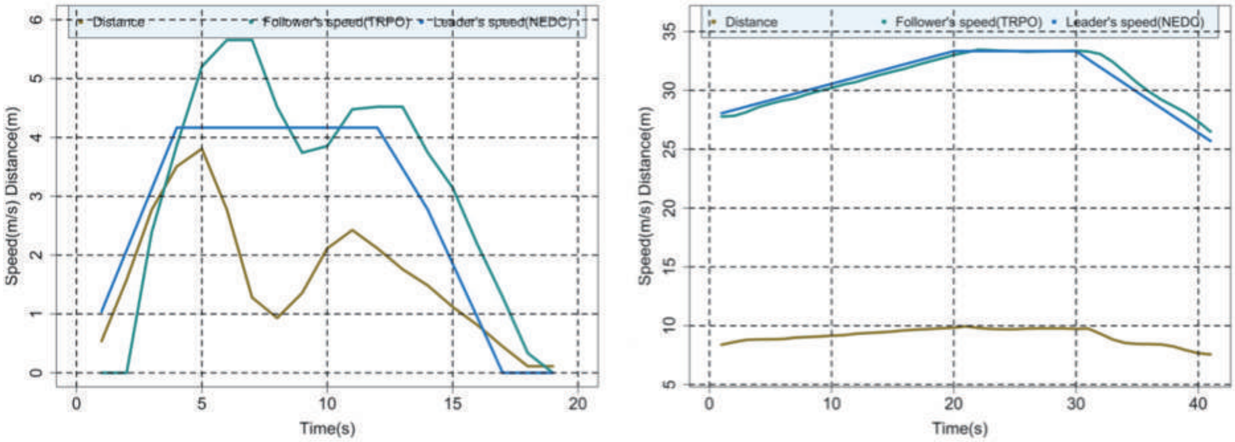

(a) The speed of follower and leader and distance between them with low speed

(b) The speed of follower and leader and distance between them with high speed

**Figure 6** The speed curves of follower (TRPO), leader (NEDC) and corresponding distance between them under two different cases

Figure 6 plots the speed curves of TRPO based follower and its distance behind the leader driving with NEDC driving cycle under two cases. From the plots, we can find that the TRPO based follower can follow the leader with a very low distance. In figure (b), the distance between the leader and follower is under 10m even the two vehicles are driving with speed above 30m/s. We can observe a 2s acceleration//deceleration duration of follower when its leader starts acceleration/deceleration. The duration does not deteriorate the driving safety, the follower can precisely control its speed and maintain the distance behind leader above 0.1m. The results indicate that the DRL based CF model is very effective. It ensures that the high speed AVs can drive with a very small gap. We can apply the DRL based CF model to autonomous platoon control, which could improve the traffic capacity. Moreover, it has been proved that the platoon with high speed and low distance can significantly reduce the air drag force of each vehicle, therefore leads to reduction of fuel consumption (Liang et.al, 2015). The proposed DRL based CF model can be further applied to longitudinal control of the platoon.

## 6. Conclusion And Future works

In this paper, we have investigated how to use DRL to CF problem of AEV with respect to electricity consumption and following distance. We build a energy consumption model of Roewe E50 using real-world data. The CF problem is formulated as a MDP, then it is solved by TRPO- a popular DRL framework. Lastly, we compared our DRL based CF approach with conventional CF models in following standard driving cycle NEDC, which suggest that our model is better than traditional models in terms of electricity consumption and following distance.

The obtained results have assumed only two vehicles interact with each other. However, in reality, traffic is commonly a significant factor in longitudinal control since it will affect the possibilities to form CF pairs and the potential electricity savings. Therefore, it is of interest to extend the DRL based driving behaviour control to more complex traffic environment. Furthermore, it is believed that the air drag force will be significantly reduced in a platoon. The application of DRL on platoon control will be a valuable future direction. Moreover, the aerodynamic forces modelling for simulation of DRL based driving control is also very important, which could tell us the optimal vehicle distance to reduce fuel/electricity consumption.

## 7. Aacknowledgements

The work was supported by national natural science foundation of China (61620106002 and 5170520). The authors acknowledge the help of Renzong Lian, who has helped us to perform traffic simulation using SUMO. The parameters of Roewe E50 is provided by SAIC Motor.

## References

[1] Arulkumaran, K., Deisenroth, M. P., Brundage, M., & Bharath, A. A. (2017). A brief survey of deep reinforcement learning. arXiv preprint arXiv:1708.05866.
[2] Chandler, R. E., Herman, R., & Montroll, E. W. (1958). Traffic dynamics: studies in car following. Operations research, 6(2), 165-184.
[3] Chong, L., Abbas, M. M., Flintsch, A. M., & Higgs, B. (2013). A rule-based neural network approach to model driver naturalistic behavior in traffic. Transportation Research Part C: Emerging Technologies, 32, 207-223.
[4] He, Z., Zheng, L., & Guan, W. (2015). A simple nonparametric car-following model driven by field data. Transportation Research Part B: Methodological, 80, 185-201.
[5] Hongfei, J., Zhicai, J., & Anning, N. (2003, October). Develop a car-following model using data collected by" five-wheel system". In Intelligent Transportation Systems, 2003. Proceedings. 2003 IEEE (Vol. 1, pp. 346-351). IEEE.
[6] Huang, X., Sun, J., & Sun, J. (2018). A car-following model considering asymmetric driving behavior based on long short-term memory neural networks. Transportation Research Part C: Emerging Technologies, 95, 346-362.
[7] Khodayari, A., Ghaffari, A., Kazemi, R., & Braunstingl, R. (2012). A modified car-following model based on a neural network model of the human driver effects. IEEE Transactions on Systems, Man, and Cybernetics-Part A: Systems and Humans, 42(6), 1440-1449.
[8] Liang, K. Y., Mårtensson, J., & Johansson, K. H. (2016). Heavy-duty vehicle platoon formation for fuel efficiency. IEEE Transactions on Intelligent Transportation Systems, 17(4), 1051-1061.
[9] Lillicrap, T. P., Hunt, J. J., Pritzel, A., Heess, N., Erez, T., Tassa, Y., ... & Wierstra, D. (2015). Continuous control with deep reinforcement learning. arXiv preprint arXiv:1509.02971.
[10] Maerivoet, S., & De Moor, B. (2005). Cellular automata models of road traffic. Physics reports, 419(1), 1-64.
[11] Mnih, V., Kavukcuoglu, K., Silver, D., Rusu, A. A., Veness, J., Bellemare, M. G., ... & Petersen, S. (2015). Human-level control through deep reinforcement learning. Nature, 518(7540), 529.
[12] Mnih, V., Badia, A. P., Mirza, M., Graves, A., Lillicrap, T., Harley, T., ... & Kavukcuoglu, K. (2016, June). Asynchronous methods for deep reinforcement learning. In International conference on machine learning (pp. 1928-1937).
[13] Onori, S., Serrao, L., & Rizzoni, G. (2016). Hybrid electric vehicles: Energy management strategies. Berlin Heidelberg: Springer.
[14] Punzo, V., Ciuffo, B., & Montanino, M. (2012). Can results of car-following model calibration based on trajectory data be trusted?. Transportation Research Record, 2315(1), 11-24.
[15] Salimans, T., Ho, J., Chen, X., Sidor, S., & Sutskever, I. (2017). Evolution strategies as a scalable alternative to reinforcement learning. arXiv preprint arXiv:1703.03864.
[16] Schmidhuber, J. (2015). Deep learning in neural networks: An overview. Neural networks, 61, 85-117.
[17] Schulman, J., Levine, S., Abbeel, P., Jordan, M., & Moritz, P. (2015, June). Trust region policy optimization. In International Conference on Machine Learning (pp. 1889-1897).
[18] Schulman, J., Wolski, F., Dhariwal, P., Radford, A., & Klimov, O. (2017). Proximal policy optimization algorithms. arXiv preprint arXiv:1707.06347.
[19] Silver, D., Huang, A., Maddison, C. J., Guez, A., Sifre, L., Van Den Driessche, G., ... & Dieleman, S. (2016). Mastering the game of Go with deep neural networks and tree search. nature, 529(7587), 484.
[20] Wang, X., Jiang, R., Li, L., Lin, Y., Zheng, X., & Wang, F. Y. (2018). Capturing car-following behaviors by deep learning. IEEE Transactions on Intelligent Transportation Systems, 19(3), 910-920.
[21] Zheng, J., Suzuki, K., & Fujita, M. (2013). Car-following behavior with instantaneous driver–vehicle reaction delay: A neural-network-based methodology. Transportation research part C: emerging technologies, 36, 339-351.
[22] Zhou, M., Qu, X., & Li, X. (2017). A recurrent neural network based microscopic car following model to predict traffic oscillation. Transportation research part C: emerging technologies, 84, 245-264.

# Development and Application of Quality Control System for Highway Subgrade Construction

**Tong Wang**

Jiangsu Easttrans Engineering Detection CO., LTD, Jiangsu Province, 210000

*Corresponding Author: Wang Tong; Four Floors of Building A2, Zidong International Creative Park, Qixia District, Nanjing; njdjwangt@126.com

## Abstract

The compaction quality of the subgrade is directly related to the service life of the road. Effective control of the subgrade construction process is the key to ensuring the compaction quality of the subgrade. Therefore, real-time, comprehensive, rapid and accurate prediction of construction compaction quality through informatization detection method is an important guarantee for speeding up construction progress and ensuring subgrade compaction quality. Based on the function of the system, this paper puts forward the principle of system development and the development mode used in system development, and displays the development system in real-time to achieve the whole process control of subgrade construction quality.

**Keywords:** *subgrade construction; compaction quality; control system; full process control*

## Introduction

In recent years, our province has been developing rapidly in terms of expressway, national highway and municipal engineering construction. However, in the project quality management, due to the lack of necessary information technology means, the construction process of some important processes cannot be monitored in real-time. For example, the subgrade construction in the sandy soil distribution areas in the coastal areas of jiangsu province has higher requirements on the quality control of subgrade compaction, while the traditional construction mainly relies on the personal experience of the roller operator, which is easy to cause leakage pressure and overpressure, and the construction quality is difficult to be guaranteed. Specifically, the following problems exist:

(1)The construction management adopts the method of paper recording, the efficiency is low and the construction inspection data cannot be obtained and utilized in real-time, which is not conducive to the future engineering management and quality problem traceability;

(2)Subgrade rolling operation process completely depends on the operator's responsibility and driving experience, which can not guarantee the strict and accurate implementation of the rolling scheme;

(3)On-site supervision adopts the way of side stations for supervision, which lacks efficient and convenient supervision means and data support;

(4)Traditional subgrade compaction degree detection is point sampling inspection method, which has large workload and limited coverage, and has certain destructive effect on subgrade filling, so it is impossible to quickly judge unqualified areas of rolling compaction.

## 1. Overall structure design of the system

The real-time monitoring system for subgrade compaction quality of high-grade highway is mainly composed of beidou Corse reference station, rolling monitoring terminal, data and application server, remote (or on-site) monitoring client and on-site PDA (mobile phone). Using the Internet of Things and Internet technology to obtain the thickness of the subgrade during real-time rolling, the rolling speed, the number of passes and the CMV value of the road roller, and use the multivariate nonlinear regression method to establish the compaction degree prediction value (CEIC) based on these four indicators, finally the construction quality of subgrade compaction process is obtained. The overall architecture of the system is shown in Figure 1.

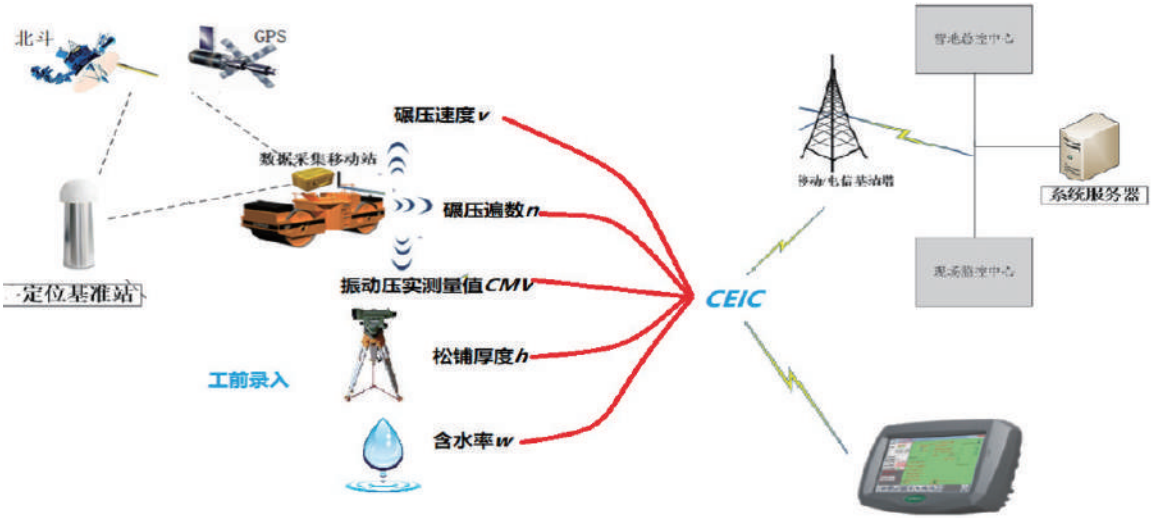

Figure 1 Overall framework of real-time monitoring system for compaction quality of high-grade highway subgrade

## 2. System composition

The system consists of subgrade construction data acquisition intelligent equipment, positioning system and subgrade construction quality control system.

### 2.1 Subgrade construction data acquisition intelligent equipment

During the rolling process, the eccentric mass block in the vibratory roller rotates, and the vibrating wheel begins to vibrate, generates vibration acceleration. The signal collected by the acceleration sensor is analyzed and processed, and the time-domain acceleration curve is obtained. In the initial stage of rolling of the subgrade, when the filling layer is loose, the vibration time domain curve is an ideal sinusoidal curve due to the small road stiffness. As the number of rolling passes increases, the filling layer becomes denser and its stiffness gradually increases. At this time, the subgrade filling layer begins to produce harmonic frequency, and the ratio of its amplitude to the fundamental frequency amplitude can be used as an evaluation index parameter for the compaction quality of the subgrade. ECV is obtained by spectral analysis of the acceleration of two or more vibration period of the vibratory wheel, the output value is the average of multiple. The indicator is related to the vibration wheel parameters (vibration wheel diameter and width) and the vibration wheel motion parameters (frequency, amplitude, speed), and it is a dimensionless parameter. As the stiffness of the compacted pavement increases, the vibrating wheel produces different harmonic components. The ECV can be used to monitor the dynamic response of the vibratory wheel compaction, reflecting the characteristics of the material being compacted. The calculation formula for ECV is:

$$ECV = \frac{A_{2\Omega}}{A_{\Omega}}$$

Type: ECV—— Quality index of continuous compaction;

$A_{\Omega}$—— Acceleration amplitude of base frequency;

$A_{2\Omega}$—— Acceleration amplitude of the second harmonic component.

The intelligent equipment for data acquisition in subgrade construction adopts the embedded standard module structure system. The acceleration sensor is a preamplifier circuit that adopts a method of amplifing the charge. Generally, the output from the sensor end is the charge with weak signal and inconvenient to be monitored. The amplifier is to amplify its output charge, reduce the impedance, and convert the charge into a voltage (voltage is easy to measure) output for easy monitoring. The signal conditioning circuit module filters the acceleration signal. The A/D acquisition module can carry out A/D acquisition transformation for acceleration signal. The CPU module analyzes and processes the acceleration signal and velocity signal. Finally, the results and related content are displayed through the screen.

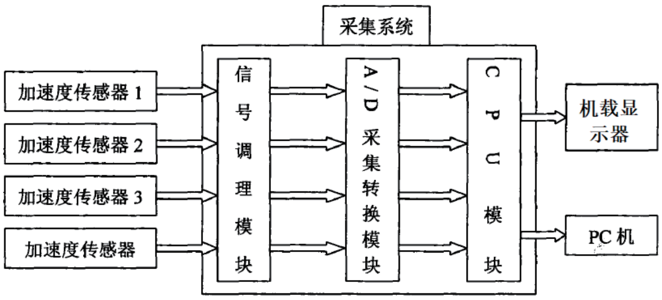

**Figure 2** Design scheme of continuous intelligent compaction monitoring device

## 2.2 Positioning system

This system adopts beidou +GPS RTK high-precision positioning technology, which is a dynamic adjustment and difference real-time solution technology developed on the basis of beidou positioning technology and ordinary RTK positioning algorithm. According to the actual situation of locking satellites in the current environment, it conducts unified deployment and calculation, avoids the phenomenon of GPS signal instability in the domestic, and provides the carrier phase algorithm of beidou to obtain the centimeter-level positioning capability. Then, based on Beidou+GPS RTK high-precision positioning technology, the corresponding roller compaction trajectory algorithm and rolling pass algorithm are developed.

### *2.2.1 Research on roller track algorithm*

The rolling track of the roller is composed of the line segments formed by the roller position at every 1s interval, and its rendering can be realized by Bresenham algorithm in line segment generation technology. The rolling area is a rolling strip formed by rolling track as the axis and extending vertically to both sides with half the width of the rolling wheel. It can be regarded as a line segment whose line width is equal to the width of the rolling wheel, and it can be drawn by using the moving brush method. The implementation method is as follows: a square brush is adopted, and the brush width is set to a value representing the width of the grinding wheel, and then move the brush center along the track segment to generate the corresponding rolling strip. In addition, the travel trajectories of different roller compactors are represented in different colors to facilitate differentiation.

### *2.2.2 Research on the algorithm of rolling pass number*

The intelligent positioning speed measuring device is installed at the center position of the roller roof (ie, the center position of the rolling roller), assuming the roller width W. Figure 3 is a schematic diagram of the calculation of the number of rolling passes. Real-time determination of roller rolling region in t, namely rectangular region ABCD, then the coordinate of point A is (Xj, Yj+W/2) and the coordinate of point B is (Xj, Yj-W/2), that is, the width range of calculation of rolling pass is yj-w /2 to Yj+W/2.

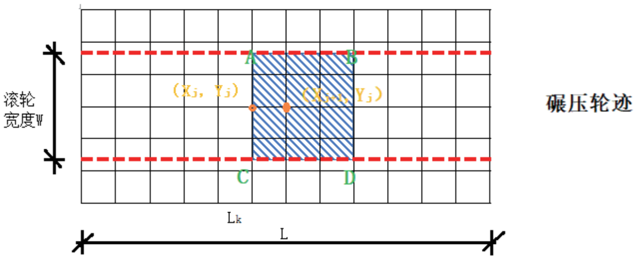

**Figure 3** Schematic diagram of the calculation of the number of rolling passes

The specific algorithm is as follows:

(1) Obtain the beidou +GPS high-precision differential positioning data and determine whether it is valid. If the result is yes, store the valid data according to the time of collection and proceed to the next step. Otherwise invalid data will be deleted.

(2) The longitude and latitude coordinate data in the stored beidou +GPS high-precision difference positioning data are transformed from the spherical coordinate system to the plane rectangular coordinate system XOY.

(3) Based on the data storage time sequence, select the initial point M (Xm, Ym) in this batch of data, and calculate the point N (Xn, Yn) that is furthest from the initial point M (Xm, Ym) in this batch of data.

(4) The XOY plane rectangular coordinate system for calculating the number of times is established, and the beidou +

GPS high-precision difference positioning data in the XOY plane rectangular coordinate system is transformed.

(5) Project all the points in the rectangular coordinate system of the XOY plane to the X-axis or Y-axis, obtain the points on the coordinate axis (Xj, 0) or (0, Yj), and form one-dimensional data values.

(6) According to the observed length interval l set externally, the acquisition and test point $l_k$ with equal spacing is set on the coordinate axis of the rectangular coordinate system of the XOY plane.

(7) The coordinate values (Xj, 0) and (Xj+1, 0) or (0, Yj) and (0, Yj+1) of the coordinate points of all adjacent moments are sequentially multiplied with $l_k$.

(8) Determine whether the coordinate values (Xj, 0) and (Xj+1, 0) or (0, Yj) and (0, Yj+1) of all adjacent coordinate points are distributed on both sides of the point according to the plus or minus of the multiplied values. If the product is negative, the two points are distributed on both sides of the acquisition test point, and the number of compaction times of the roller at the current section position is added by 1. If the product is positive, the two points are on the same side, and the number of compaction times of the roller at the current section position is unchanged. Traverse all points, obtain the road roller construction times of the road section passing the point $l_k$.

(9) Determine whether it is the last cross-section position. If the judgment result is yes, output the number of construction that need to observe the cross-section, and then the program stops and waits for the next start. Otherwise, the calculation of the next cross-section construction number is continued.

## 2.3 Subgrade construction quality control system

### *2.3.1 Design principle*

(1) Suitability

"Data security" is the primary design principle. The architecture not only meets the industry's "data privacy requirements", but also meets the "functional requirements" such as simplicity and convenience of use.

(2) Stability

The system structure fully considers the stability of the system, and the design is guaranteed to ensure the stable operation of the system for 7×24 hours. Operation interface design, database design, module design, data structure design and so on should also fully consider the stability of the system.

(3) Openness

The system design follows the open principle, the system has a strong secondary development ability, can be further developed according to future development needs.

(4) Maintainability

The system structure is simple, modular programming technology is adopted, and the software configuration is simple and effective. All configuration actions have corresponding configuration interface and relevant description information, ensuring the convenience of system update, maintenance and upgrade.

(5) Flexible expansion

The system software adopts the structure system of layered development and multi-point network communication. The dynamic library is mainly connected between the functional modules in each device, forming the system running state of low coupling and high cohesion. Intelligent interface technology and reserved perfect data interface are adopted to realize the docking with other information systems. At the same time, the system will not destroy the stability of the original structure when it is extended and upgraded or function modified.

(6) High performance

Through the application of caching and load balancing technology, the maximum utilization rate of resources should be less than 70%, and the average utilization rate of resources should be less than 50% when the system is running within 7×24 hours. The WEB server can be accessed by 1000 users at the same time, and the WEB page access speed is no more than 3 seconds; The terminal positioning data upload interval of 5 seconds, the system has the processing capacity of 1500 pieces of positioning data information per second on average and 2500 pieces of positioning data information per second at peak.

(7) Load balancing

The system application adopts the distributed business processing and storage mode of multi-communication front machine and multi-service server, and the database adopts the horizontal partition mode to achieve load balance. And has the ability to expand the system capacity only by increasing the number of corresponding servers. Without having to make major adjustments and changes to the system.

*2.3.2 System objectives and functions*

System objectives

(1) On-line real-time monitoring of project construction quality.

(2) The integrated management of quality monitoring and progress information during highway construction provides information application and support platform for highway construction quality and progress control, as well as highway safety diagnosis.

(3) To achieve the owners and supervisors of the project construction quality of deep participation, fine management. Through the automatic monitoring of the system, not only the owner can rest assured of the project quality, effectively control the construction progress, but also can realize the rapid response to the highway construction quality and progress control.

(4) It provides an information integration platform for the completion acceptance, safety appraisal and future operation and management of highway construction.

System implementation functions

(1) The software is composed of monitoring center, field sub-control station, GPS reference station, network system and roller device monitoring terminal, etc. It mainly realizes the following functions:

(2) The digital model of highway section is established, and the rolling parameters and rolling area are monitored in real-time based on the digital model. Dynamic monitoring of subgrade rolling machinery track, speed and rolling height.

(3) Real-time automatic calculation and statistics of subgrade at any location of the rolling times, compaction thickness, etc., and in the subgrade construction digital map visualization display, at the same time for online query.

(4) When the roller is overspeed, the system automatically sends alarm information to the operator, site supervisor and construction management personnel. When the number of rolling times and compaction thickness are not up to the standard, the system will prompt the detailed content and the location of the coordinates that are not up to the standard, which will be reflected in the software platform of the control system, so as to timely instruct adjustment or rework, and write the alarm information into the construction abnormal database for future reference.

(5) After the construction of each layer, graphic report of rolling quality is output, including rolling track chart, rolling times chart, compaction thickness chart and compaction elevation chart, etc., which are used as auxiliary materials for quality acceptance.

The rolling quality information of all construction sections during the construction period is saved to the network database.

## 3. Display system

### 3.1 Rolling speed status

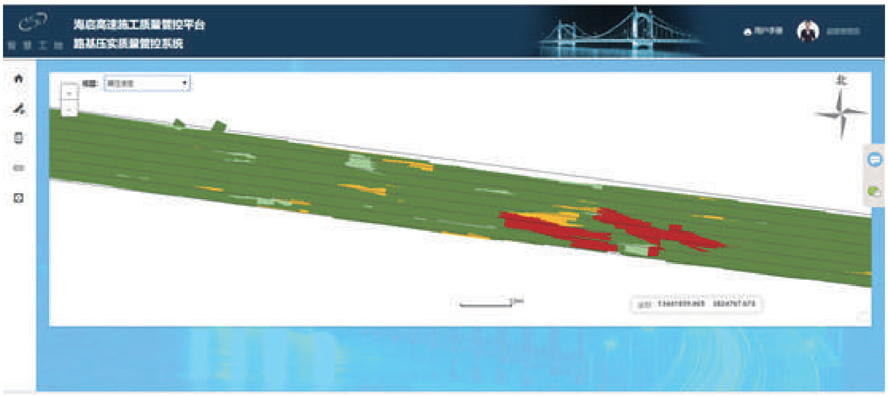

**Figure 4** Rolling speed

### 3.2 Rolling times state

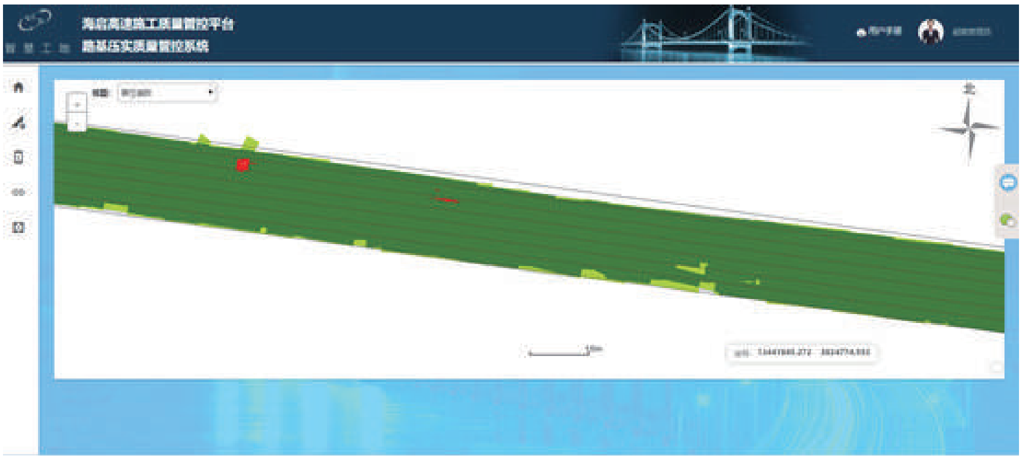

**Figure 5** Rolling times

### 3.3 Compaction quality report

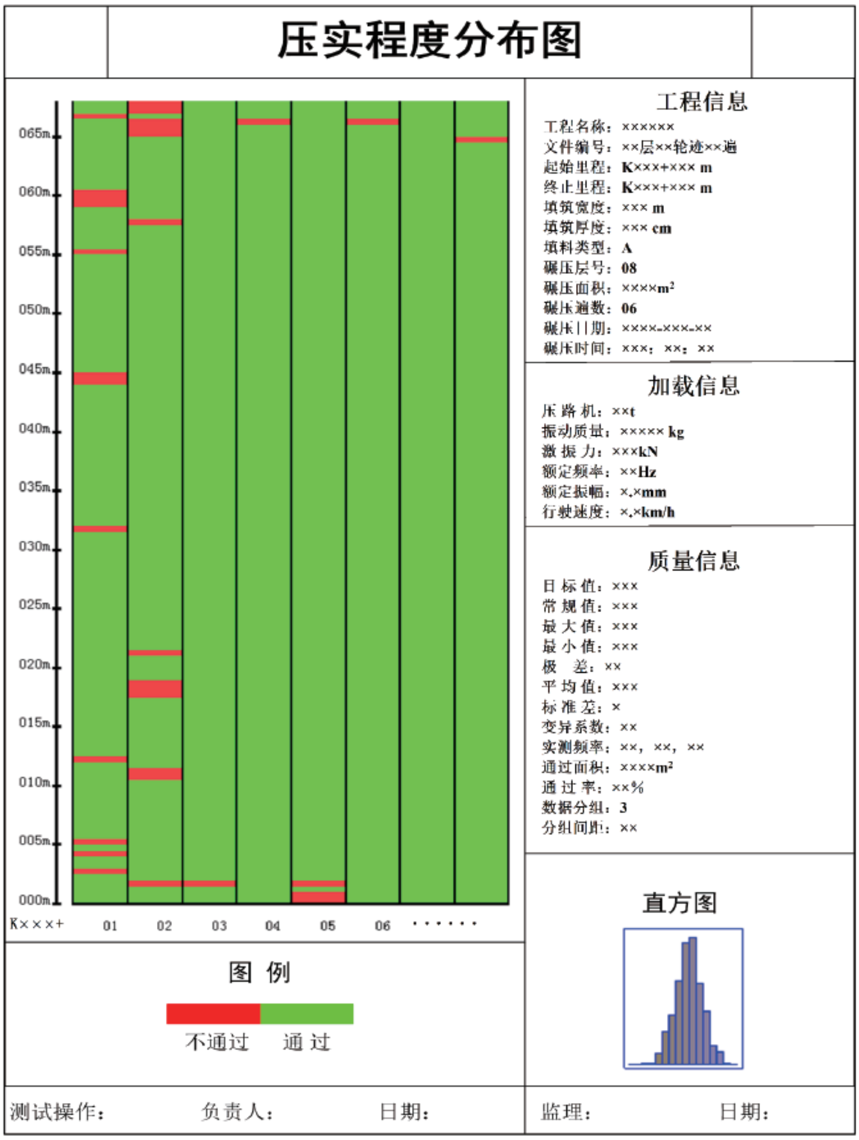

压实程度分布图

工程信息

工程名称：××××××
文件编号：××层××轮迹××遍
起始里程：K×××+××× m
终止里程：K×××+××× m
填筑宽度：××× m
填筑厚度：××× cm
填料类型：A
碾压层号：08
碾压面积：××××m²
碾压遍数：06
碾压日期：××××-×××-××
碾压时间：×××：××：××

加载信息

压 路 机：××t
振动质量：××××× kg
激 振 力：×××kN
额定频率：××Hz
额定振幅：×.×mm
行驶速度：×.×km/h

质量信息

目 标 值：×××
常 规 值：×××
最 大 值：×××
最 小 值：×××
极　差：××
平 均 值：×××
标 准 差：×
变异系数：××
实测频率：××，××，××
通过面积：××××m²
通 过 率：××%
数据分组：3
分组间距：××

直方图

图 例

🟥 不通过　🟩 通 过

测试操作：　负责人：　日期：　监理：　日期：

**Figure 6** Compaction quality report

## 4. Social and Ecnomic Benefits

### 4.1 Ecnomic Benefits

Asphalt pavement is now the main form of highway pavement structure in China. Beacause of the insufficient bearing capacity of subgrade, net-shaped cracks, longitudinal cracks, subsidence rutting and other diseases appear. Pavement damage directly affects the safety of driving and leads to traffic jam. From the research, it shows that once the degree of compaction increase by 1%, the modulus of resilience of earth subgrade increase by 2.5%, thus we can know that the increase in degree of compaction will obviously increase the strength of the earth subgrade and improve the service life of the subgrade. For Expressways and Second Class highways, 1% decrease of the degree of compaction will lead to 0.5 years decrease in road life. For Expressways, the design life decreases by 3.3% for 15 years, for Second Class highways, the design life decreases by 4.2% for 12 years, and for tertiary highways, the degree of compaction decreases by 1%, the road life decreases by 0.3 years and the design life decreases by 3.8% for 8 years. This section takes expressway as the object of economic benefit analysis.

The cost of a single set of equipment in this system is 60,000 yuan, which can be reused many times (use 2 times as sample). Based on the calculation of 5 rollers on site, 5 sets of vehicle-mounted equipment are needed. The platform fee and maintenance fee of the expressway subgrade construction quality management and control system are 200,000 yuan per project. On calculation of half of the cost of a single set of equipment and the cost of system platform and maintenance, the total cost of the system is 5 x 3 + 20 = 350,000 yuan. According to the engineering experience mentioned above, it can be estimated that the economic loss is about 230,000 yuan per kilometer, accounting for 3.3% of the cost of road surface, for every 1% decrease in the degree of compaction of subgrade.

**Table 1** Analysis of Influences of Subgrade Compactness on Full Life Cost of Asphalt Pavement

(Bi-directional and Six lane) Unit(10000yuan)

| Cost per kilometer of Asphalt Pavement | The annual cost of a single kilometre based on 15-year life expectancy | The life of road that shortened once the compactness of subgrade is reduced by 1% | Economic loss per kilometer caused by 1% reduction of subgrade compactness |
|---|---|---|---|
| 700 | 46 | 0.5 | 23 |

This set of Expressway subgrade construction quality management and control system can effectively reduce the economic losses caused by rework due to unqualified degree of compaction. Table 2 conservatively estimates the construction cost of subgrade per kilometre to be 380,000 yuan. If the loss caused by rework is considered, the rework cost per kilometre is 3080 yuan according to 1% rework rate. In the absence of this system, if the degree of compaction is increased by one percentage point by using this monitoring system, the benefit will be increased by 230,000 yuan per kilometer. Therefore, the total economic benefit of 10 kilometer long pavement will be (23+0.308)*10=23,308,000 yuan. The investment-benefit ratio (cost-effectiveness ratio) of the Expressway subgrade construction quality control system is 35/233.08=0.15.

**Table 2** Estimation of unit price of subgrade construction(28m Wide) Unit(1000yuan/km)

| Labor costs | Machinery fee | Charges | Construction cost per kilometre | Rework fee (Rework rate 1%) |
|---|---|---|---|---|
| 5.6 | 5.6 | 19.6 | 30.8 | 0.308 |

### 4.2 Social Benifits

This compaction monitoring system focuses on process control, real-time display and record construction parameters such as rolling times, rolling quality, rolling detection date and time. In the construction process, real-time operation guidance is provided for the constructors. The constructors and supervisors can find out whether the construction process parameters meet the technical requirements of the construction specifications in real time, and correct the unsatisfactory operation parameters and operation modes in real time. They can do traditional detection in the compacted weak areas which will improve the qualified rate of one-time detection and save the cost of the inspectors. The use of this system can greatly improve the efficiency of compaction operation while ensuring the construction quality and by visual display interface, even drivers without rich construction experience can achieve precise control and shorten the construction time. It can also eliminate the rework caused by leakage pressure, less pressure and over pressure, reduce the waste of resources and time, and improve the quality of subgrade construction which can extend road service life and reduce the cost of later maintenance.

## 5. Conclusion

(1) Introduced the overall architecture design of the system and the hardware composition of the system, providing a basis for the development of the system.

(2) Starting from the function of the system, the whole process of monitoring data acquisition, storage and final application is analyzed, and the principle of system development and the development mode used in system development are put forward.

(3) The quality management and control system of expressway subgrade construction is developed. By inputting the thickness of construction loose and acquiring the ECV, rolling speed and rolling times in real time, the whole process of subgrade construction quality is controlled, and the remote real-time inquiry of rolling speed, rolling times and compacting quality can be achieved.

(4) Through the analysis of social and economic benefits, adopting the quality management and control system of expressway subgrade construction can bring remarkable social and economic benefits.

## References

[1] Wu Yongping. Analysis of Intelligent Compaction Technology System[J]. Construction Mechanization, 2012, (6): 41-44.

[2] Gong Shutao. Development and application of real-time monitoring system for roadbed compaction quality of high-grade highway [D]. Tianjin University, 2014.

[3] Yu Liang, Zhang Zhiyuan. Discussion on GPS Measurement Technology in Road Engineering[J]. Science & Technology Vision, 2014, (4): 113-114.

[4] Tu Huiying, Pan Yinglong. Discussion on roadbed compaction[J]. Communications Science and Technology Heilongjiang, 2010, (11):31-33.

[5] Wang Haiyan, Yang Fangting, Liu Lu. Comparison and Application of Standardization Coefficient and Partial Correlation Coefficient[J]. The Journal of Quantitative & Technical Economics, 2006(09): 150-155.

[6] Jinsang Hwang, Hongsik Yun, Juhyong Kim. Development of Soil Compaction Analysis Software (SCAN) Integrating a Low Cost GPS Receiver and Compactometer [J]. Sensors, 2012, (12):2351-2353.

[7] Lee, H.K. An integration of GPS with INS sensors for precise long-baseline kinematic positioning [J]. Sensors 2010, 10:9424–9438.

# Treatment on Crumb Rubber Modifier towards Enhanced Storage Stability of Asphalt Rubber

**Guocheng Su, Jiangmiao Yu, Mijash Vaidya***

School of Civil Engineering and Transportation, South China University of Technology, Wushan Road, Tianhe District, Guangzhou 510000, China;

*Corresponding Author: *Mijash Vaidya, mijashvaidya@gmail.com;*

## Abstract

Breaking waste tires into crumb and adding it to asphalt as modifier to prepare asphalt rubber (AR) is an effective method to solve the waste tire problem and improve the performance of matrix asphalt. The modified asphalt has better high and low temperature performance. However, the segregation of the crumb rubber modifier (CRM) causes storage instability of the AR. At present, studies have been conducted that improving the solubility of the CRM or adding some macromolecular polymer can improve the storage stability of the AR. However, the structure and polarity of the CRM surface are rarely explored for its correlation with the storage stability of AR. In this paper, the surface structure and polarity of the CRMs was changed by four different reagents, and the properties of the ARs prepared by the CRM were measured to analyze the adhesion between the CRM and the asphalt. It is concluded that the CRM with rough porous and non-polar surface has higher storage stability due to the better interfacial adhesion, which provides a research direction for improving the storage stability of rubber asphalt.

**Keywords:** *storage stability; asphalt rubber; interfacial adhesion; polarity*

## 1. Introduction

The development of the automobile transportation industry has promoted economic and social progress, but considerable waste tires have hindered social development [1]. The irrational treatment of waste tires can lead to serious problems for society and human health [2]. The recycling of waste tires is the key to solve this problem. Among it, the preparation of asphalt rubber (AR) by crushing waste tires into crumb rubber modifier (CRM) and then adding it to matrix asphalt is the main market for recycling waste tires.

As early as 180 years ago, CRM began to be tested on asphalt pavement. In the 1960s, "dry process" and "wet process" were successively invented, and AR began to be widely used and studied [3]. Compared with matrix asphalt, AR has high-temperature stability, low temperature crack resistance, and also better aging resistance. The asphalt mixture produced by AR is also so superior in performance that it is the most important binder in road construction, especially for the flexible pavement. [4].

However, due to the instability of thermodynamics, the CRM as a modifier always exhibits segregation during storage, which destroys the modification effect of the CRM. Especially when the binder is stored at high temperatures, the expanded CRM settles rapidly due to the higher initial density than asphalt [5]; In addition, some studies have shown that the density of the CRM after swelling is reduced and migrates to the top of the asphalt [6] . Ghavibazoo analyzed the effect of the dissolution of the CRM on the final properties of the binder and found that the percentage of dissolution affected the storage stability of the AR [7]. However, the dissolved CRM will lose the effect of the modification. At present, there is little research on the correlation between the adhesion of CRM and asphalt interface to the storage stability of AR.

In order to solve the storage instability in the process of compatibility between CRM and asphalt, this paper proposes the correlation between the surface structure and polarity of CRM in the process of modifying asphalt according to the principle of “similar compatibility”. The surface of the wet-crushed 80-mesh waste tire CRM was treated with four different reagents including sodium hydroxide, carbon tetrachloride, silane coupling agent (KH-Si69) and sodium hypochlorite. Measurements are carried to characterize the surface of CRM by scanning electron microscopy, infrared spectrometer and surface contact angle tester. Then the CRM before and after treatment is prepared to make AR, and the modification effect is obtained by various performance indexes before and after Rolling Thin Film Oven (RTFO). The evaluation was carried out to evaluate the interfacial adhesion characteristics of CRM and asphalt.

The conclusion is drawn that the adhesion between the CRM and the asphalt interface is not only related to the polarity of the CRM surface, but also the microstructure of the CRM. In addition, different chemical agents also affect the performance of AR. It is initially believed that a rough porous and hydrophobic non-polar surface facilitates an increase in adhesion between CRM and asphalt. The improvement of surface structure and polarity of CRM can be used as a research direction to improve the storage stability of AR.

## 2. Material and Experiment Design

### 2.1 Material

Compared with ambient shredding[8] and cryogenic grinding, the wet-processed CRM is the most suitable to modify asphalt for its rough surface and uniform small size [3]. Therefore, the wet-processed CRM with a size of 80 mesh was used in this study. The penetration of the matrix asphalt is 7.0mm, which is commonly used in Guangdong. In addition, four chemical reagents including 5 mol•L$^{-1}$ sodium hydroxide solution, carbon tetrachloride, KH-Si69, and sodium hypochlorite solution were used.

The KH-Si69 solution is prepared according to the ratio of coupling agent: water: absolute ethanol = 1:1:20, and standing for 2 hours to ensure sufficient hydrolysis of the coupling agent.

The sodium hydroxide solution, carbon tetrachloride, KH-Si69 solution and sodium hypochlorite solution were respectively reacted with CRM in an oven at 50℃ for 2 hours, and the obtained CRMs were labeled as RA, RB, RC, and RD. The untreated CRM is recorded as RO.

The AR was prepared by the "wet process". The specific operation process was as follows: 800 g of matrix asphalt was preheated in an oven at 180℃ for 40 min, and then slowly mixed up with 144 g of RO, RA, RB, RC, and RD respectively under the stirring of the shearing machine for 20 min with the 1400 r / min of rotation speed; and then the rotation speed of the shearing machine slowly increased to 4500 r / min and keep shearing for 40 min; finally the rubber swelled in the asphalt at 180-185℃ for 4 h, and the AR obtained is recorded as O, A, B, C and D.

### 2.2 Test methods

#### *2.2.1 CRM test*

The scanning electron microscope (SEM) test utilizes the high-energy electron beam obtained by the aggregation to bombard the surface of the CRM, and the physical signals obtained after the interaction is used to characterize the microscopic morphology of the surface of the CRM. In this study, SEM test was carried out with a scanning electron microscope S-3700N at Hitachi Company in Japan with an operated voltage of 10 kV. Before tested, the sample should be placed on a metal stage for gold spraying.

When the substance is irradiated with infrared light, if the frequency of the infrared light is consistent with the vibration frequency of the functional group of the material molecule, a resonance effect occurs, and the substance absorbs infrared light of a specific frequency, and then the transmittance of the infrared light is reduced at that frequency. The functional group is analyzed by the transmittance of infrared light of the sample. In this study, a Fourier transform infrared spectrometer (FTIR) VERTEX 70 manufactured by Bruker Company in Germany was used under a wavelength of 400 ~ 4000 cm$^{-1}$. The samples were compressed by KBr tableting method.

The contact angle can be used to judge the wettability of the solid as well as the polarity of the solid surface. In this study, the surface contact angle tester OCA40 Micro produced by the German Dataphysics Company was used. The test liquid was distilled water with a droplet volume of 4 μL and a droplet velocity of 1μL/s.

#### *2.2.2 AR test*

The physical properties of AR were tested by penetration, softening point and ductility test. Workability was characterized by the rotational viscosity measured using a Brookfield digital viscometer at 135℃ and 165℃ to provide a reference for asphalt mixing and compaction temperatures.

The penetration was determined by the inserting depth caused by a 100 g stylus inserted into a pitch at 25℃ for 5 s, and the viscosity of the asphalt could be further evaluated by this value. The softening point was represented by the temperature at which the small steel ball slides down to the bottom with the asphalt sample on the small steel ring from 5℃ , and this could also evaluate the high temperature stability of the asphalt. Further, the asphalt was stretched at a stretching speed of 5 mm/min at 5℃ until fracture, and the tensile length at the time of breaking was the ductility of the asphalt, evaluated for the deformation resistance and low temperature performance. The aging resistance of asphalt was evaluated by the physical properties including penetration and ductility which had been aged by RTFO.

For storage stability, an isolation experiment was used for evaluation. During the experiment 50 g of AR was poured into the sample aluminum tube, sealed and placed in an oven at 163℃ for 48 h, and then placed in a refrigerator for freezing. After the asphalt solidification, it was divided into two sections, and the difference between the softening points of the top and down section was measured. This value was used to evaluate the segregation of the AR, and further used as a basis for evaluating the compatibility between CRM and matrix asphalt.

## 3. Result and Discussion

### 3.1 CRM

#### *3.1.1 SEM test result*

The change in shape, size, and aggregation of the CRM with and without the treatment can be seen from figure 1.

It can be seen in figure 1(a) that with the treatment by sodium hydroxide, the size of the CRM is obviously increased, and the degree of aggregation becomes larger. Compared with the CRM without treatment, those treated by carbon tetrachloride and KH-Si69 seem that there is no obvious change; while the CRM treated by sodium hypochlorite was obviously reduced both in size and the degree of aggregation.

In figure 1(b), the CRM treated with sodium hydroxide has pin-like particles gathered on the surface of the CRM. The one treated with carbon tetrachloride has a smoother surface for the guess that carbon tetrachloride is related to the dissolution of impurities on the surface of the CRM. The surface of the CRM treated by the KH-Si69 is rough and porous. It is because some of the hydroxyl groups of the coupling agent are dehydrated into bonds with the hydroxyl groups on the surface of the CRM after hydrolysis, and adhered to the surface of the CRM. For the CRM treated with sodium hypochlorite, due to the strong oxidizing property which can completely oxidize some unsaturated groups, the surface becomes smoother and have fewer holes.

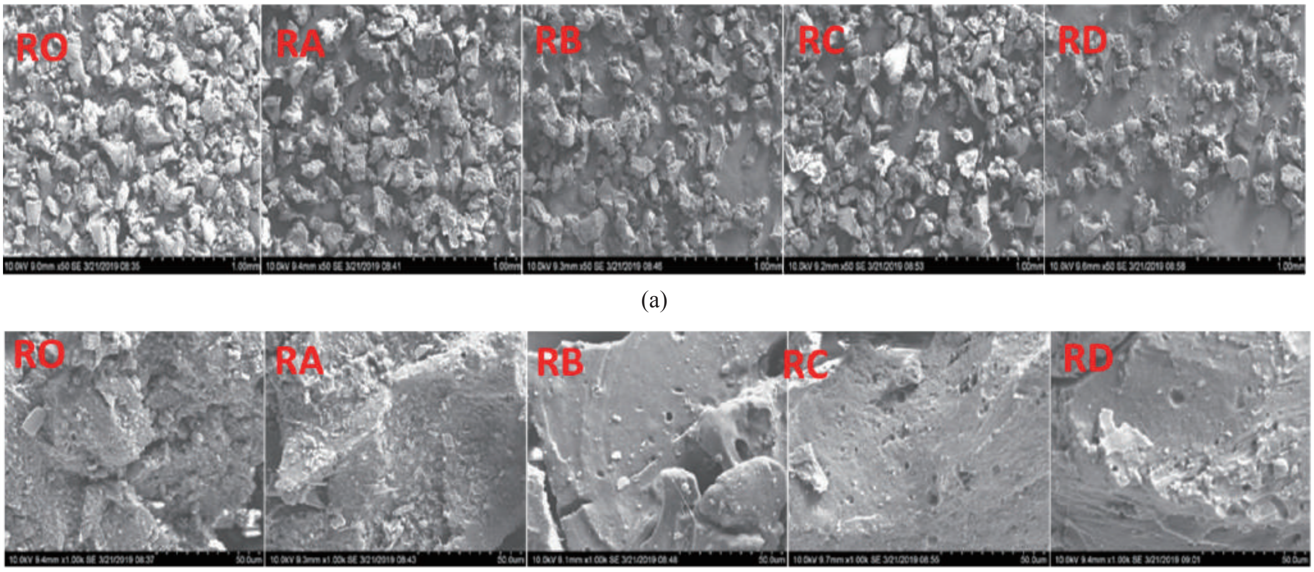

(a)

(b)

**Figure 1**. SEM evaluation: (a) 50 times; (b) 1000 times.

#### *3.1.2 FITR test result*

Figure 2.(a) is the infrared spectrum peak of CRM, and Figure 2.(b) is the analysis of the main peak position. After chemical treatment, the CRM was decolorized to some extent, making the infrared spectrum peak more obvious. At the wave numbers of 3500cm$^{-1}$ and 1636cm$^{-1}$, the peak intensity of the infrared spectrum is: RD>RA>RB>RC. Therefore it is

speculated that the surface polarity of the CRM treated with sodium hypochlorite becomes the largest while the one treated by KH-Si69 has the smallest polarity. A similar pattern exists in the fingerprint area of about 600 cm$^{-1}$.

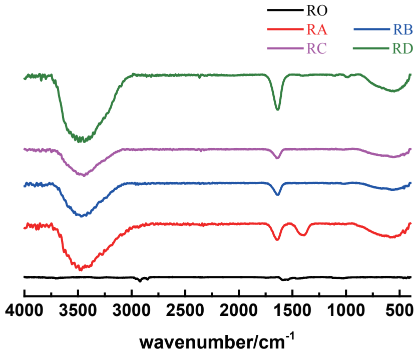

(a)

Main functional groups in CRM:

3500 cm$^{-1}$ (O-H the stretching vibration of hydroxyl group),

1636 cm$^{-1}$ (C=O stretching vibration of carbonyl group),

1400 cm$^{-1}$ (O-H in-plane bending vibration of alcoholic hydroxyl group).

(b)

**Figure 2**. FTIR evaluation of CRM: (a) spectrum; (b) analysis.

### *3.1.3 contact anger test result*

By measuring the contact angle of the interface, the hydrophilicity or hydrophobicity of the CRM can be known and the polarity change of the CRM can be estimated. It can be seen from table 1 that the surface change effect of the CRM is different after different treatment. The surface of the CRM treated with carbon tetrachloride and KH-Si69 becomes more hydrophobic than the original CRM while those treated with sodium hydroxide and sodium hypochlorite have a hydrophilic surface. For RD, the water droplets are completely extended on the surface of it as long as it contacts with the water droplets. So the contact angle with water cannot be accurately measured by this method.

**Table 1**. Interface contact angle between CRM and water.

| - | RO | RA | RB | RC | RD |
|---|---|---|---|---|---|
| test 1 | 128.7° | 82.17° | 133.5° | 139.9° | - |
| test 2 | 129.8° | 81.3° | 135.0° | 140.4° | - |
| test 3 | 129.6° | 77.0° | 134.1° | 139.1° | - |
| average | 129.4° | 80.2° | 134.2° | 139.8° | - |

This is also consistent with the above infrared analysis results. The more -OH , more hydrophilic, and the more polarity. The CRM treated with carbon tetrachloride or KH-Si69 has a significantly larger interface angle with water than the untreated one , which indicated a smaller polarity.

## 3.2 AR

### *3.2.1 Physical properties before RTFO*

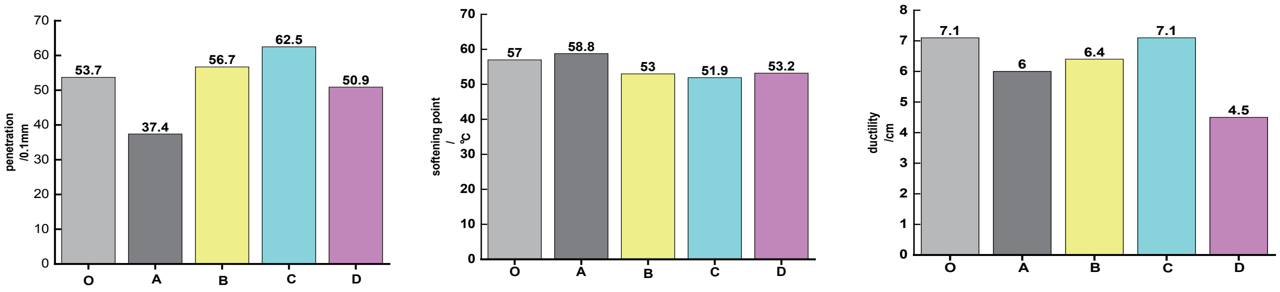

(a) (b) (c)

**Figure 3**. Physical properties before RTFO: (a) penetration; (b) softening point; (c) ductility.

As the penetration shown in Figure 3 (a), after the sodium hydroxide treatment, the penetration of A is significantly reduced, followed by D. The penetration of the B or C is improved, and the increase in the C is the most obvious, increased by 16%. It shows that the CRM treated with carbon tetrachloride and coupling agent has better compatibility with the matrix asphalt.

As shown in Figure 3 (b), except for the group treated with sodium hydroxide, the softening points of the other groups has decreased. But overall, the change in softening point is not significant. It shows that different reagent has little effect on the high temperature stability of AR.

The ductility is basically reduced as shown in Figure 3 (c), the magnitude of the decrease is D>A>B>C=O. Note that in addition to the KH-Si69 treatment group, other treatment methods will reduce the low temperature performance of the AR.

### *3.2.2 Workability*

As shown, the viscosities at 135℃ and 165℃ show the same pattern, i.e. A > O > B > C > D. That is to say, in addition to the fact that the sodium hydroxide treated sample increases the viscosity of the AR while other agents lowers the rotational viscosity of the AR at 135℃ and 165℃. The decrease in viscosity indicates that the workability of the AR prepared by the treated CRM is improved.

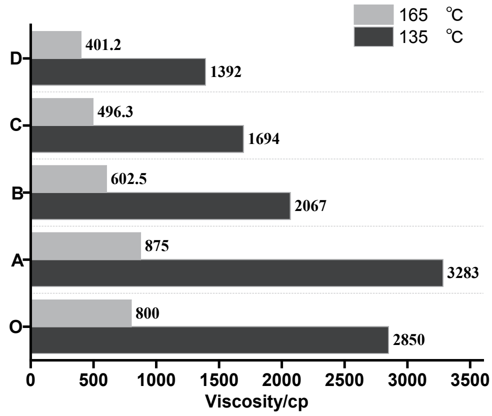

**Figure 4**. Rotational viscosity test results.

### *3.2.3 Storage stability*

The storage stability of the AR was evaluated by the separation test of the asphalt binder. Figure 5 shows the softening point difference between the top and bottom section of the sample. It can be seen that the AR treated by the KH-Si69 can significantly improve the storage stability, and other treatment methods are generally effective. As known before, the surface of the CRM treated by KH-Si69 is rough and porous, and the specific surface area is relatively large so that the contact area with the matrix asphalt is larger. At the same time, the surface of the CRM treated by KH-Si69 is less polar as the asphalt, which makes the CRM treated by this reagent is better compatible with the matrix asphalt and has better interfacial adhesion properties.

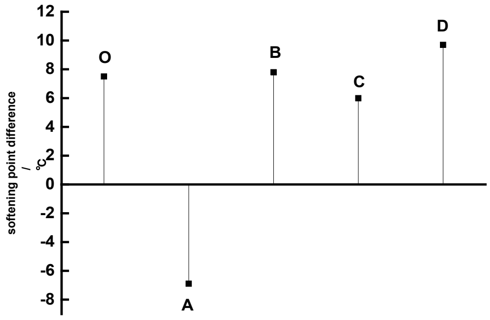

**Figure 5**. Storage stability of AR.

### *3.2.4 Physical properties after RTFO*

The penetration ratio of various ARs before and after RTFO is shown in Figure 6(a). It shows that the penetration ratio of the AR treated with the reagent is higher than that of the untreated one.

Figure 6(b) is a comparison of the 5 °C ductility before and after RTFO. After RTFO, all the ARs showed a decrease in ductility, and the AR prepared by the untreated CRM had the smallest degree of decline, among which the AR treated with KH-Si69 had the largest decrease in ductility. From the perspective of ductility, the aging resistance of various ARs is as follows, O>B>A>D>C.

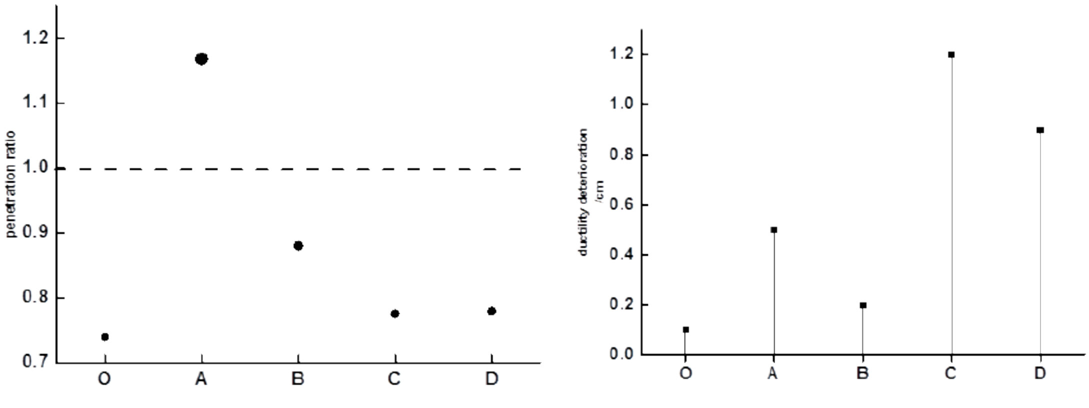

(a) (b)

**Figure 6**. Physical properties before RTFO: (a) penetration ratio; (b) ductility deterioration.

## 4. Conclusions

In order to solve the problem of storage instability in the process of compatibility between CRM and asphalt, this paper proposes the correlation between the surface structure and polarity of CRM in the process of AR according to the principle of “similar compatibility”. The treatment method makes the CRM have different surface structure and polarity, and then the following conclusions by measuring the physical properties are obtained.

- The CRM treated with sodium hydroxide or sodium hypochlorite reagent has an increased surface polarity, becomes more hydrophilic, increases the degree of aggregation, which is not compatible with asphalt.
- The surface of the CRM treated with carbon tetrachloride or KH-Si69 becomes more hydrophobic and non-polar. Among them, the surface of the KH-Si69 -treated CRM is rough and porous, and the storage stability of the AR prepared by this CRM is significantly improved. While the surface of the carbon tetrachloride treated CRM is smooth and less porous, making the interface adhesion effect with the asphalt not ideal.
- The CRM treated with sodium hydroxide and sodium hypochlorite exhibits a modification effect different from that of other reagents, and its mechanism needs further investigation.

The adhesion between the CRM and the asphalt is not only related to the polarity of the surface of the CRM, but also the microstructure. It is initially believed that a rough porous and hydrophobic non-polar surface facilitates an increase in adhesion between CRM and asphalt. In addition, different chemical agents will also affect the performance of the modified asphalt, and the influence mechanism of different chemical reagents will be further explored. How to improve the storage stability of AR, and how to reduce odor and optimize the working environment by improving the interface adhesion of CRM and asphalt, will become a major development direction of AR.

**Acknowledgments:**The authors sincerely acknowledge the funding support from the National Natural Science Foundation of China (No.51678251) and the Fundamental Research Funds for the Central Universities (NO. SCUT.2018KZ001). Trademark or manufacturers’ names appear in this paper only because they are considered essential to the object of this paper.

## References

[1] Madhusudhan B R, Boominathan A, Banerjee S. Properties of Sand–Rubber Tire Shreds Mixtures for Seismic Isolation Applications, 2019[C] .

[2] Chen C C, Yamada T, Chiu I M, et al. Evaluation of the Waste Tire Resources Recovery Program and Environmental Health Policy in Taiwan[J]. International Journal of Environmental Research & Public Health, 2009,6(3):1075-1094.

[3] Lo Presti D. Recycled Tyre Rubber Modified Bitumens for Road Asphalt Mixtures: A literature Review[J]. Construction and Building Materials, 2013,49:863-881.

[4] Jeong K, Lee S, Amirkhanian S N, et al. Interaction Effects of Crumb Rubber Modified Asphalt Binders[J]. Construction and Building Materials, 2010,24(5):824-831.

[5] Navarro F J, Partal P, Martínez-Boza F, et al. Thermo-rheological Behaviour and Storage Stability of Ground Tire Rubber-modified Bitumens[J]. Fuel, 2004,83(14-15):2041-2049.

[6] Pérez-Lepe A, Martínez-Boza F J, Gallegos C. High Temperature Stability of Different Polymer-modified Bitumen: A Rheological Evaluation[J]. Journal of Applied Polymer Science, 2007,103(2):1166-1174.

[7] Ghavibazoo A, Abdelrahman M. Composition Analysis of Crumb Rubber During Interaction with Asphalt and Effect on Properties of Binder[J]. International Journal of Pavement Engineering, 2013,14(5):517-530.

[8] Sienkiewicz M, Borzędowska-Labuda K, Zalewski S, et al. The Effect of Tire Rubber Grinding Method on the Rubber-asphalt Binder Properties[J]. Construction and Building Materials, 2017,154:144-154.

# ITDP-Robot: Design of An Intelligent Transport Dispatch Parking Robot

**Sanqing Qu*, Zhongcong Xu, Fan Lu, Guang Chen, Zhuoping Yu**

College of Automotive Engineering  Tongji University, Shanghai, China

## Abstract

In this paper, a novel electric autonomous parking robot prototype was proposed, which aims to address the parking hassle caused by the imbalance between the vehicle ownership and the amount of the parking spaces. The mechanical structure was elaborately designed to allow the parking robot to adapt to vehicles with different wheelbases and tracks. The electrical structure was constructed with the aim of X-by-wire and distributed component-based control concept. To be capable of autonomous driving, the parking robot software system based on ROS was designed with the capability of environment perception, self-localization and path planning. Furthermore, a simulation environment based on Gazebo was built in order to simplify the development of the parking robot's autonomous driving algorithms and validate those algorithms' robustness. Though this parking robot is under the prototype stage, the dispatch strategy and the convenience for parking were also considered. Compared with the state-of-art parking robot, this parking robot is not only capable of working indoor parking lots but also the complex outdoor environments.

**Keywords:** *parking robot, mechatronic design, autonomous driving system, simulation and application*

## 1. Introduction

According to global vehicle ownership and vehicle production statistics, the vehicle ownership is steadily increasing. Hao et al. (2011) proposed a hybrid model of China's vehicle ownership, by using this model, they projected that China's vehicle population would reach 184.8, 363.8 and 606.7 million by 2020, 2030 and 2050 respectively. With the increase in vehicle ownership, parking has become an increasingly severe social issue especially in China, due to the shortage of parking spaces and the "information island" effect. In most instances, searching for a suitable parking space demands time consumption. Furthermore, a long search for an available parking space in a highly congested scenario might induce exhaustion, tension or even traffic accidents. Hence, to alleviate this problem, Jaurkar et al. (2016), Kotb et al. (2017), Latif et al. (2018) and Zhu (2018) developed and implemented intelligent parking guidance systems to provide the drivers with information about the availability of parking spaces.

In the past few years, with the rapid development of artificial intelligence (AI), the research and development of autonomous driving vehicles have made great progress. Besides, X-by-wire chassis is also undergoing a rapid development, as Eder et al. (2010), Sens (2013), Zong et al. (2013), Ni et al. (2018) shown, the next generation of automobiles will increasingly incorporate electronic control units (ECUs) and X-by-wire chassis in novel automotive control applications. Especially, steer-by-wire has many potential applications due to its superior flexibility, as Luo et al. (2017) and Zhang et al. (2017) shown, four-wheel steering and four-wheel drive (4WS4WD) electric vehicle (EV) is of higher maneuverability and flexibility which is prerequisite for valet parking and self-driving. In this social context, intelligent parking technology has become a research hotspot, competitive focus and application breakthrough point in the field of autonomous driving. As Schwesinger et al. (2016), Banzhaf et al. (2017), Kang et al. (2017) and Huang et al. (2018) shown, the realization of automated valet parking (AVP) enables the vehicle to drive to a parking spot and park itself, which allows passengers to leave the car in a drop-off zone. And It is believed that AVP system has great potential to mitigate the parking headache for the future smart city. However, due to the prohibitive cost of sensors and technical maturity, most ordinary vehicles cannot be equipped with this functionality. Besides, to realize the automatic parking for the cars equipped with these facilities, parking lots must be upgraded to meet the demand of automatic parking technology. But it's inevitable that there are some different requirements among the different automatic parking technology solutions. Therefore, to adapt to different technical specifications, the renovation and transformation to the traditional parking lots are too challenging.

To address these difficulties, as He et al. (2016) previously shown, the fully automatic parking lot equipped with automatic parking robot is designed creatively. With the assistance of autonomous parking robots, the parking process can be tremendously simplified, which makes the autonomous parking available for the traditional vehicles. The customer does not need to park by himself/herself anymore. They only need to park the car at a transfer station and then submit a parking request to the parking lot system, after that, a parking robot will carry the vehicle to a suitable parking space assigned by the dispatch system. And the pick-up process is nearly the same as the parking process. To reduce the unnecessary waiting time at the transfer station, the customer can even make a reservation of the picking up process. There is no doubt that the development of automatic parking lots can significantly improve parking safety and convenience. Furthermore, the automatic parking lot can dramatically improve the utilization efficiency of space, which means the automatic parking lots can accommodate much more vehicles than the traditional parking lots. Hence, it is reasonable for us to believe that this field of technology is of great prospect.

Within the scope of this paper, the next section briefly describes some relevant state of the art parking robots and followed by a detailed illustration of the mechanical design of our parking robot in section III. After that, in section IV the parking robot's electrical design is presented, and section V illustrates the design of the autonomous driving system. Section VI describes the simulation results of the parking robot in a specific virtual parking lot. Then in section VII, we introduce the application about our parking robot. The conclusion in the last Section ends this work.

## 2. State of The Art

Meanwhile, quite a few companies are offering or at least announcing innovative parking robot or concepts. For instance, as the Web-1 presents, the Yee Fung company in Shenzhen, China, developed the latest generation of AGV parking robot -- GETA, which has a payload of 2.6 tons and a maximum speed of 1.5 m/s. It can store and retrieve almost all passenger vehicles. The average cost of time is less than 120 seconds. Besides, as the Web-2 presents, the SERVA Transport Company, Germany, whose latest generation of RAY™ parking robots, has a maximum transport load of 3 tons and a maximum travel speed of 3 m/s. This Robot is also capable of handling almost all passenger vehicles.

**Figure 1**. Tongji autonomous parking robot prototype "ITDP-Robot".

However, still, these robots are only able to be applied in indoor parking lots, outdoor parking lots are too complicated to be handled due to the complex environments. Our contribution to this trend is the setup of a novel electric autonomous parking robot, characterized by comprising two lateral and a transverse stretch and folding apparatuses, with the aim of adapting to the wheelbase and tread of different vehicles. The parking robot is designed to carry vehicles from one position to a given spot without human intervention, with the capability of environment perception, self-localization and path planning, and can be competent for the outdoor parking lots. The prototype of our autonomous parking robot is shown in Figure 1.

In what follows, the task to build our autonomous parking robot prototype based on four-wheel steering with the capability of adapting to the complex outdoor environments was described in detail.

## 3. Mechanical Design

The mechanical system of the parking robot consists of the following parts: body, traction units, steering drive unit, stretch and folding unit and elevating unit. Among them, the traction units provide the driving power of this parking robot and control the traveling direction; the steering drive unit can improve the steering performance; stretch and folding unit allows the parking robot to adapt to vehicles with different wheelbases and tracks; elevating unit is used for holding the wheel and lifting the vehicle. With the help of these units, our parking robot can lift and transport vehicles of different sizes.

### 3.1 Body

The body is the basis of the entire mechanical structure, and all units will be mounted on the body to achieve its function. The body of the vehicle is welded by steel pipes, and fine mechanical simulations are performed to ensure its strength and rigidity. As Figure 1 shows, the body of the parking robot consists of four parts connected by stretch and folding unit: front-left part, front-right part, rear-left part and rear-right part. The traction units are mounted on the front two parts and the steering drive unit on the rear two parts. In addition to this, an extra universal wheel is mounted on each part to improve the mechanical properties and elevating unit is also installed on each part to lift the vehicle.

### 3.2 Traction Drive Unit

The traction drive unit illustrated in Figure 2, is based on a permanent magnet synchronous motor which is mounted horizontally. Allow for the heavy weight of the parking robot, the polyurethane wheels are applied, of which the maximum load is 1800kg. The traction motor and a traction gearbox with a gear ratio of 1:29.3 are integrated and coupled with the wheel. After the reduction of the traction gearbox, the nominal wheel torque is up to 225Nm and can guarantee that a certain gradient can be overcome. Besides, a rotary encoder (E40H10-1024-3-T-5, Autonics) that has a resolution of 1024 p/r provides the prerequisites for the realization of the closed loop speed control of the traction motor.

**Figure 2**. Integration of Traction and Steering Unit.

### 3.3 Steering Drive Unit

The steering drive unit was divided into two different parts. The front steering drive unit is integrated with the traction motor and polyurethane wheels perpendicularly. Actuated by a steering drive controller, the steering motor generates a torque of 1.5 Nm and a power of 400 W. The steering motor couples with the gear under the flange which can act as a reduction gear box and as a result the wheel can change the direction of the parking robot even under a heavy load that is up to 3000kg. To control the steering angle precisely, there is also a rotary encoder (E40H10-1024-3-T-5, Autonics) coupled with the shaft of the steering motor, with which the steering angle is closed-loop controlled.

Compared with the front one, the structure of the rear steering drive unit is much simpler. And a horizontally mounted permanent magnet synchronous motor can generate sufficient steering torque with a gearbox. This special gearbox can record the absolute steering angle of the rear wheels even though the power is switched off suddenly, which guarantees security after an unexpected halt caused by emergencies.

### 3.4 Stretch and Folding Unit

With the revolution of stepper motors can both of the lateral and longitudinal stretch and folding units move precisely to adjust according to the variant track and wheelbase of different cars. Lead screws with right and left-hand thread are adopted in the unit and the lead of the thread is carefully selected to ensure that the lead screw has self-locking characteristics so that no additional mechanical locking means are required. Linear rails are also used so that the unit can stretch or fold in a specific direction and bear the load during lifting and carrying vehicles. Lead screws and linear rails are assembled in three square tube steel welded frames which are bolted to two parts of the body, and they can move relative to each other in a specific direction to achieve the lateral and transverse stretch and folding. The strength and stiffness of lead screws, lead screws nuts, linear rails, and the frame are carefully checked to ensure that the frame does not fail even when lifting 2.5-ton cars.

### 3.5 Elevating Unit

The elevating unit is designed to clamp the wheel and lift and lay down the car slowly and steadily. For the clamping function, the worm gear mechanism is used because of its self-locking characteristics so that no additional locking mechanism is required and a stepper motor is applied to drive the arms to clamp the tires of the vehicle. In order to lift and lay down the vehicle, a servo motor and a gearbox are integrated and coupled with a ball screw which can convert the rotational motion to linear motion and the max load of each elevating unit is 10000N. On each elevating unit, there are three limit switches to guarantee the security when the car is being lifted at a maximum speed of 1 cm/s.

## 4. Electrical DESIGN

In this section, the electrical design of our autonomous parking robot is detailed illustrated, with the aim of X-by-wire and distributed component-based control concept.

### 4.1 Electrical Architecture

As we can see in Figure 3, with the aim of the convenience for components extension the electrical architecture is layered and includes distributed components. The basic electrical architecture consists of three essential components, i.e., Jetson TX2, VCU (Vehicle Control Unit), and EPEC (EPEC 3724 Control Unit). Jetson TX2, VCU and EPEC can establish half-duplex communication via CAN bus. VCU send commands to the traction drive controller, front and rear steering drive controllers, and elevating drive controllers, of which the communication protocol is customized CAN or CANopen. In reverse, the listed components can also send data to VCU. EPEC controls stretch and folding unit and receives the data sent by RC receiver with pulse via cables.

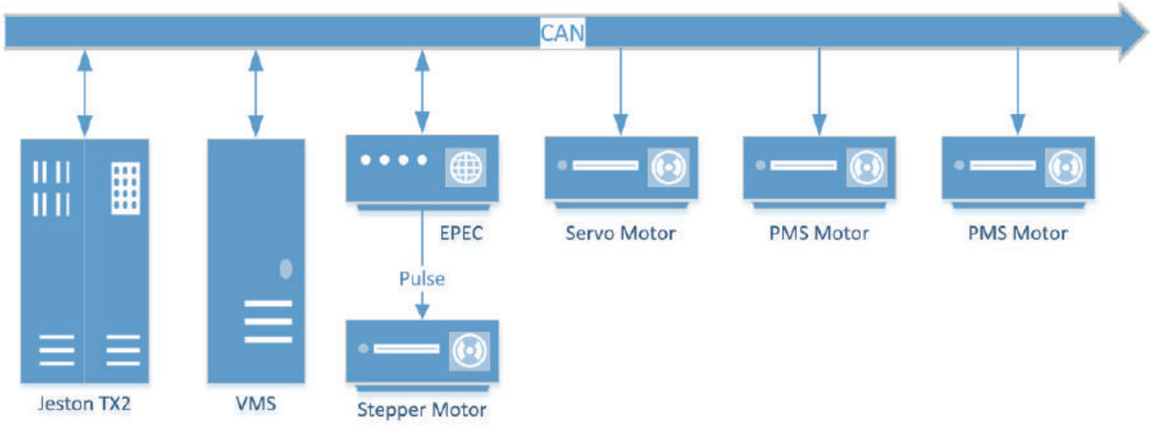

**Figure 3**. Electrical Architecture of "ITDP-Robot."

### 4.2 Power Supply Unit

The power supply unit of the vehicle is made up of 4 lead acid batteries, each of the batteries is with 12VDC. In Figure 3 the power distribution is shown. Traction motors demand 48VDC input voltage in order to actuate the traction motors that reach a maximum power of 2200W. The steer drive unit and the drive controllers in elevating and stretch unit all need 48VDC input voltage. Furthermore, a DC-DC converter transfer the voltage from 48V to 12V and as a result it can supply power for EPEC and Jetson TX2. The other components, such as sensors and limit switches are also supplied by this power unit with some other converters when necessary.

## 5. AutoNomous Driving Design

In the following, insights were given into issues concerning the autonomous driving design of our autonomous parking robot. With the aim of being competent for autonomous driving, the parking robot was designed with the capability of environment perception, self-localization and path planning. Furthermore, to achieve the target of carrying vehicles from one position to a given spot without human intervention, as a unique capability, the parking robot is also necessary to have the ability to detect and align the customer's vehicle accurately. The hardware and software design of the parking robots' autonomous driving system are illustrated in detail in following subsections.

### 5.1 Hardware Architecture

Figure 4 presents the overall hardware architecture of "ITDP-Robot". We use two NVidia Jetson TX2 to build up our core computation platform, where the two devices communicate with each other over Ethernet through a switch. The first device receives signals from the robot's vehicle control unit (VCU) and EPEC 3724 control unit(EPEC) dedicated for remote control(RC). Also, it handles real-time data from camera sensors and conducts vision detection using deep learning technique. Joint self-localization with both GNSS and Velodyne LiDARs relies on the second device, which collects all laser point cloud from all LiDARs, performing tasks like map fusion, obstacle detection and target vehicle recognition. As for the sensors, the parking robot is equipped with nine single-beam Rplidar sensors. Six of them are aimed for the detection of the customer's vehicle when the parking robot is assigned to carry the vehicle to the parking lot, and the other three are equipped to detect obstacles during the operation. The vision system is composed of four monocular cameras, which are responsible for the detection and identification of derivable areas, traffic signals, and lane markers. The two Velodyne VLP-16 scanners mounted on the front edge are designated to detect and identify obstacles and play the most important roles in self-localization and mapping.

All the sensors mentioned above are carefully calibrated and unified to one global coordinate frame, the defined parking robot coordinate frame centered at the front axle, which has been proved to be helpful for vehicle maneuvers.

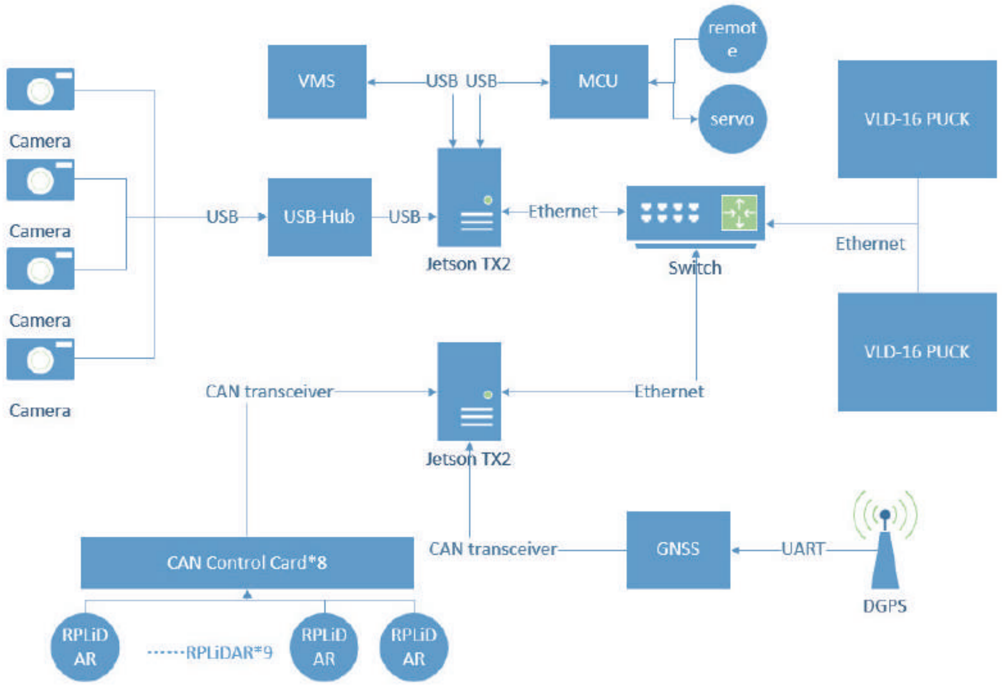

**Figure 4**. The autonomous driving system's hardware architecture of "ITDP-Robot."

### 5.2 Software Architecture

The software system of "ITDP-Robot" is implemented based on ROS and its overall architecture is illustrated in Figure 5. Each transparent rectangle represents a meta package in ROS, while every inner blue rectangle means a ROS package or a ROS node. Messages transmitted between ROS packages are shown as arrows in Figure 5. With the purpose of making every function non-interfering, the system is uncoupled in 5 independent units: Environment Perception Unit, Self-Localization Unit, Map Fusion Unit, Dispatch and Path Planning Unit and Motion Control Unit.

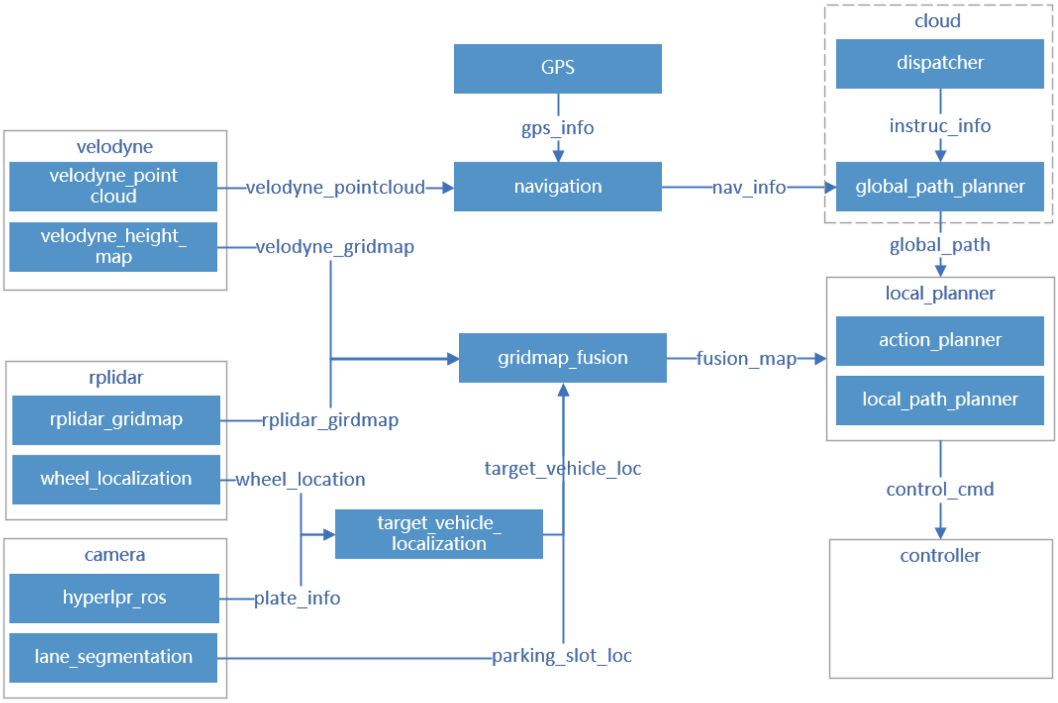

**Figure 5**. The autonomous driving system's software architecture of "ITDP-Robot."

*5.2.1 Environment Perception Unit*

The Environment Perception Unit consists of "velodyne", "rplidar" and "camera" meta packages, for receiving and processing data from 16 beams LiDAR, single beam LiDAR and camera sensors respectively. Velodyne contains 2 ROS packages, publishing point cloud messages and grid map messages (the point cloud projected to a 2D plane and filtered by height). Regarding rplidar, besides the grid map, the wheel location messages are also published, using the wheel localization method based on the L-shape feature. In the camera module, both car plate messages and parking slot messages are generated by deep learning object detection and semantic segmentation models. All of these messages are then subscribed by Self-Localization Unit and Map Fusion Unit.

## 5.3 Self-Localization Unit

The Self-Localization Unit only aims to publish global localization information messages to Dispatch and Path Planning Unit. In order to improve robustness and adaptation ability, LiDAR-dominated NDT-matching is adopted instead of GPS-dominated localization method. The general pipeline of self-localization is described as follow. Firstly, a high definition 3D point cloud map of the working area is built in advance. Then once the robot drives into the working area, an NDT (Normal Distributions Transform) algorithm will launch to get the localization information, by matching the point cloud message with the point cloud map and computing the transform matrix. Finally, an EKF (Extended Kalman Filter) is applied to fuse the localization result of NDT and GPS, and then outputs the final result.

## 5.4 Map Fusion Unit

The function of this unit is to generate a Fusion Map utilizing the message from Environment Perception Unit. For efficient message transmitting and specific message defining, the Fusion Map message consists of 3 layers: grid map layer, target vehicle location layer and parking slot location layer. Each layer is stored independent but can be transmitted together as a general fusion grid map.

## 5.5 Dispatch and Path Planning Unit

The Dispatch Unit is deployed on the cloud, subscribing the global localization message and publishing the global path for the robot. More details are mentioned in Section VII. As for Path Planning Unit, local path is planned according to the fusion grid map published by Map Fusion Unit. Every local decision also depends on Path Planning Unit such as lifting or laying down the target vehicle.

### 5.6 Motion Control Unit

With the aim of high maneuverability and flexibility, the mechanical structure and electrical structure were designed based on the X-by-wire theory. Therefore, a motion control unit was introduced to provide the interfaces between the software system and the hardware system. The motion control unit was constructed based on the closed-loop proportion integration derivative (PID) control theory. With this unit, the parking robot can response for the expected motion rapidly and smoothly.

## 6. Simulation

Allow for that the autonomous driving software architecture was constructed on ROS. To simplify the development of the parking robot's autonomous driving algorithms and validate the robustness, we have built a simulation environment on a robot simulator Gazebo, which has a robust physics engine, high-quality graphics, and convenient programmatic and graphical interfaces.

Figure 6 shows the simulation environment built in Gazebo, which is constructed based on a ratio of 1:1 to the real scenes. A close to real representation parking robot presented in Figure 6 was constructed with SolidWorks. Also, all sensors mentioned in section 5.1 were carefully configured in the simulation environment to provide sensors data as consistent as possible with the real sensors data. It is worth to mention that all the kinematic parameters were specified according to the real circumstance, and a specific script was composed to test the kinematic performance of our parking robot. Also, in this simulation scenario, the car's pick-up process with the ITDP-Robot was validated, Figure 7 presents the simulation result.

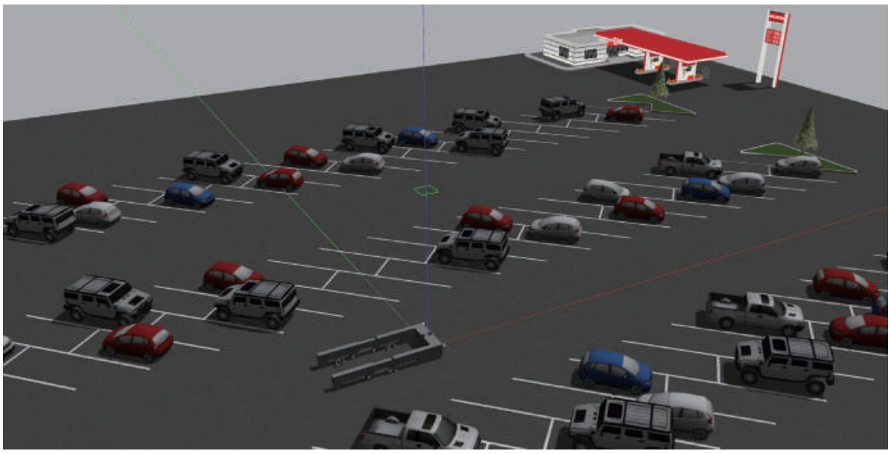

**Figure 6** Simulation environment built in Gazebo.

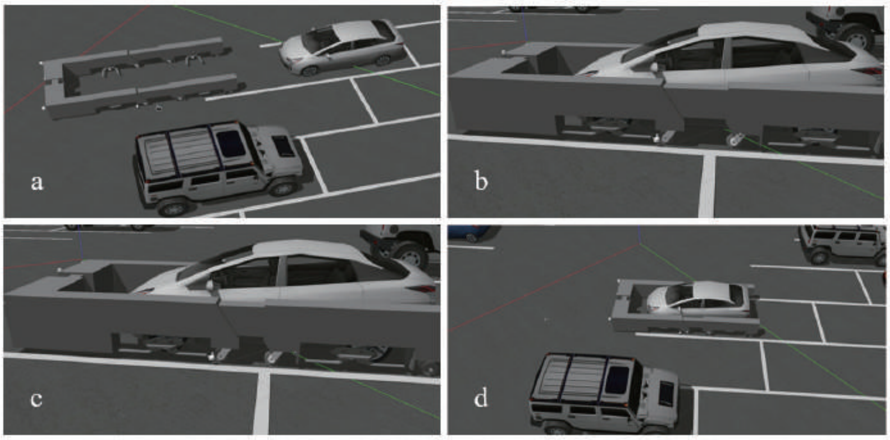

**Figure 7** The simulation for the car pick-up process with the "ITDP-Robot."

## 7. Application

In this section, the dispatch strategies and more parking and pick-up process details were presented. With intelligent and robust dispatch strategies, the automatic parking lot system can reasonably and efficiently dispatch the optimum parking robot to execute the parking and pick-up operation.

### 7.1 Dispatch Strategies

In order to complete the parking and pick-up task at the fastest speed and with minimum cost, we propose a multi-objective optimization method. We introduce 0-1 decision variables, comprehensively use the operating cost and time cost of the entire parking lot as the objective function, and based on the actual work completion logic to formulate the constraints according. Furthermore, in order to adapt to different scenarios and different tasks, the dynamic task generation strategies were introduced.

Allow for that the above scheduling problem belongs to the NP-hard problem, with the traditional algorithm to obtain the optimized dispatch strategy might consume plenty of computational time, especially as the amount of the scheduling tasks increases. To satisfy the demand of real-time scheduling, we innovatively introduced a hybrid parallel genetic algorithm, utilizing the simulated annealing algorithm to improve the accuracy and executing parallel computation on GPU to reduce the computational time.

### 7.2 Parking and Pick-up Process

Outside the parking lot, some capacious transfer stations were constructed. When the user wants to park the car, he does not need to consume time and energy to search for an available parking space anymore, only needs to stop the car at a transfer station and submit a parking request to the server. Then the parking process for the user was finished, and a parking robot will take the vehicle to a suitable parking space assigned by the dispatch system. The vehicle's information will automatically upload to the cloud server. When the user wants to pick up the car, he only needs to submit a pick-up request to the server, and then the server will assign a parking robot to take the car from the parking lots to the transfer station.

Considering that even if there are intelligent and robust dispatch strategies, due to the pick-up operation time, the customer will still have to waste some waiting time during the pick-up process. To improve the experience, a smart-phones' app was developed from scratch to help the customer to manage the car. With the assistance of this app, the customer can submit a reservation request to the server at any time. When it is time for picking up, the server will send a notice to inform the customer to confirm the pick-up request. If the customer confirms the request, the server will assign a parking robot to take the car to a suitable transfer station and feedback the transfer station's location to the app. As a result, when the customer arrives at the transfer station, the car is already there in a driving direction, and the customer will not waste time to wait for the pick-up process anymore.

## Conclusions

In this paper, with the aim of addressing the parking hassle caused by the imbalance between vehicle ownership and the number of parking spaces, we proposed a novel electric autonomous parking robot prototype. Because of the elaborately designed mechanical structure, the parking robot can adapt to cars with different wheelbases and tracks. And this parking robot can be competent for both the indoor and outdoor scenes with the assistance of the autonomous driving system based on ROS. Also with the assistance of the developed dispatch system, the automatic parking lot system will dispatch the optimum parking robot to execute the parking and pick-up operation. Since the whole system is still under the prototype stage, for further future work, we will conduct more experiments to examine the algorithms' robust and optimize the robot's mechanical structure.

## References

[1] Hao, H., Wang, H., & Yi, R. (2011). Hybrid modeling of China's vehicle ownership and projection through 2050. Energy, 36(2), 1351-1361.
[2] Kotb, A. O., Shen, Y. C., & Huang, Y. (2017). Smart parking guidance, monitoring and reservations: a review. IEEE Intelligent Transportation Systems Magazine, 9(2), 6-16.
[3] Jaurkar, H. V., Mulay, G. N., & Gohokar, V. (2016, August). Parking guidance system using Internet of Things. In Inventive

Computation Technologies (ICICT), International Conference on (Vol. 1, pp. 1-6). IEEE.
[4] Latif, S., Afzaal, H., & Zafar, N. A. (2018, March). Intelligent traffic monitoring and guidance system for smart city. In Computing, Mathematics and Engineering Technologies (iCoMET), 2018 International Conference on (pp. 1-6). IEEE.
[5] Zhu, D. (2018). Deep learning over IoT big data-based ubiquitous parking guidance robot for parking near destination especially hospital. Personal and Ubiquitous Computing, 1-8.
[6] He, T., Shao, J., Zhang, Y., Jiang, J., & Gu, B. (2016). Recent Patents on Automated Transporting Vehicle in Automatic Car Parking System. Recent Patents on Mechanical Engineering, 9(1), 2-8.
[7] Eder, M., & Knoll, A. (2010, August). Design of an experimental platform for an x-by-wire car with four-wheel steering. In Automation Science and Engineering (CASE), 2010 IEEE Conference on (pp. 656-661). IEEE.
[8] Sans, M. (2013, November). X-by-wire park assistance for electric city cars. In Electric Vehicle Symposium and Exhibition (EVS27), 2013 World (pp. 1-9). IEEE.
[9] Zong, C. F., Li, G., Zheng, H. Y., He, L., & Zhang, Z. X. (2013). Study progress and outlook of chassis control technology for X-by-wire automobile. Zhongguo Gonglu Xuebao(China Journal of Highway and Transport), 26(2), 160-176.
[10] Luo, J., Hang, P., Luo, F., Wu, L., & Chen, X. (2017, July). Sliding mode-based learning control for a novel steering-by-wire system. In Control Conference (CCC), 2017 36th Chinese (pp. 3627-3634). IEEE.
[11] Zhang, Z., Zhang, X., Pan, H., Salman, W., Rasim, Y., Liu, X., ... & Li, X. (2017). A novel steering system for a space-saving 4WS4WD electric vehicle: design, modeling, and road tests. IEEE Transactions on Intelligent Transportation Systems, 18(1), 114-127.
[12] Ni, J., Hu, J., & Xiang, C. (2018). Control-Configured-Vehicle Design and Implementation on an X-by-Wire Electric Vehicle. IEEE Transactions on Vehicular Technology, 67(5), 3755-3766.
[13] Banzhaf, H., Nienhüser, D., Knoop, S., & Zöllner, J. M. (2017, June). The future of parking: A survey on automated valet parking with an outlook on high density parking. In Intelligent Vehicles Symposium (IV), 2017 IEEE (pp. 1827-1834). IEEE.
[14] Huang, C., Lu, R., Lin, X., & Shen, X. (2018). Secure automated valet parking: A privacy-preserving reservation scheme for autonomous vehicles. IEEE Transactions on Vehicular Technology, 67(11), 11169-11180.
[15] Schwesinger, U., Bürki, M., Timpner, J., Rottmann, S., Wolf, L., Paz, L. M., ... & Heng, L. (2016, June). Automated valet parking and charging for e-mobility. In Intelligent Vehicles Symposium (IV), 2016 IEEE (pp. 157-164). IEEE.
[16] Kang, D. H., Kang, C. M., Kim, J. S., Kim, S., Kim, W. Y., Lee, S. H., & Chung, C. C. (2017, October). Vision-based autonomous indoor valet parking system. In Control, Automation and Systems (ICCAS), 2017 17th International Conference on (pp. 41-46). IEEE.

# Modeling Interstation Travel Speed of Hybrid Bus Rapid Transit within A Bayesian Framework

**Ji-hua Hu,** [1*]**, Jia-xian Liang**[2]

1 Public Labs Center, Sun Yat-sen University, Guangzhou 510006, China
2 Research Centre of Intelligent Transportation System, School of Engineering, Sun Yat-sen University, Guangzhou 510006, China

*Corresponding Author: Ji-hua HU, Ph.D., Public Labs Center, Sun Yat-sen University, Guangzhou 510006, China

## Abstract

Interstation travel speed is an important indicator of the running state of hybrid Bus Rapid Transit and passenger experience. Due to the influence of road traffic, traffic lights and other factors, the interstation travel speeds are often some kind of multi-peak and it is difficult to use a single distribution to model them. In this paper, a Gaussian mixture model charactizing the interstation travel speed of hybrid BRT under a Bayesian framework is established. The parameters of the model are inferred using the Reversible-Jump Markov Chain Monte Carlo approach (RJMCMC), including the number of model components and the weight, mean and variance of each component. Then the model is applied to Guangzhou BRT, a kind of hybrid BRT. From the results, it can be observed that the model can very effectively describe the heterogeneous speed data among different inter-stations, and provide richer information usually not available from the traditional models, and the model also produces an excellent fit to each multimodal speed distribution curve of the inter-stations. The causes of different speed distribution can be identified through investigating the Internet map of GBRT, they are big road traffic and long traffic lights respectively, which always contribute to a main road crossing. So, the BRT lane should be elevated through the main road to decrease the complexity of the running state.

**Keywords:** *bayesian, hybrid BRT, RJMCMC, interstation travel speed, gaussian mixture model*

## 1. Introduction

The travel speed is the main advantage of the Bus Rapid Transit (BRT) over ordinary buses, especially in the downtown area, but the speed of the hybrid BRT system may have some difference. Hybrid BRT is an improved form of BRT, which has facilities such as bus lanes, new public transport stations and intelligent monitoring and management systems, but is no longer isolated from ordinary bus lines (1). Ordinary buses are free to enter and exit the BRT system, passengers can transfer to the buses in station, private cars in the off-peak hours can also runs into some part of the BRT lanes, which enhances the efficiency of the city's overall bus system. But these changes will also have great impact on the interstation travel speed of hybrid BRT, and the distribution of the travel speed will be more complexed. The interstation travel speed is an important indicator of the running state and efficiency of the BRT (2). It is also the main input data of BRT simulation. Therefore, it is necessary to model the speed and analyze the running state of hybrid BRT consequently.

The travel speed was usually modeled with a normal or lognormal distribution, or a Gaussian mixture distribution with a fixed K value (3). However, the travel speed of hybrid BRT is affected by more factors, including road traffic, traffic lights, and other factors. Therefore, the distribution of travel speed varies largely between stations, often showing multi-peak phenomenon; and the influence factors of different interstation are not the same, accordingly the distributions must be different, so it is difficult to use the above model to describe them. Therefore, constructing a mathematical model describing the multi-peak travel speed of interstation of hybrid BRT is very necessary.

In addition to the single mathematical model mentioned above, other scholars had proposed different types of distribution to model the non-normality of the sampled travel speed. Dey and others showed that the speed data could follow a unimodal or a bimodal curve depending on the variation of speed for different categories of vehicles (4). A similar approach taken by Ko and Guendsler characterized the congestion based on the two mixtures of speed distribution. They assumed that the speed distribution over a given time had a form of mixed distribution, one for congested and the other for uncongested flow (5). Some researchers had adopted Gaussian mixture models to cluster transport-related observations into groups and discovered the existence of multi-regime states. Park et al. employed the model to account for heterogeneity in speeds based on actual data collected from an existing highway segment. Jun utilized the model to characterize the severity and variability of congestion on certain interstate roadway systems (6). Corey et al. (2011) used a Gaussian mixture model to identify the sensitivity errors of inductive loop detectors (7). More recently, Lao et al. also utilized a Gaussian mixture model to estimate traffic speeds and classify vehicle volumes using measurements from single-loop detectors (8). However, Park et al. did not fully incorporate the parameter (i.e. the number of components) into the Bayesian framework to infer other unknown parameters. The Bayesian framework assumes that the number of Gaussian mixture models and the parameters of each component to be random variables and to have their own certain prior distribution (9). And the posterior distribution of these parameters needs to be estimated. The commonly used parameter estimation method was the RJMCMC method (10), such as Lee, which used this method to determine the component number of the Gaussian mixture model of the subway passenger's travel time data and the parameters of each component, and then determined the whole Gaussian mixture model (11).

bus station-reporting data refers to when the bus stops at the station and open the door, it reports the station to the passengers and reminds the passengers to get off; when the bus doors closed, it reminds other passengers the next station, so they can be ready for getting off. Bus station-reporting data is generated during the process. From the data, the travel time between neighbored stations can be extracted, then the interstation travel speed can be computed. In this paper, the interstation travel speed is calculated using the station-reporting data of a hybrid BRT. Then, within a Bayesian framework, the Gaussian mixture model is used to model the interstation travel speed, and the number of model components is estimated using the RJMCMC method, so do the parameters of each component. Finally, combined with the impacts of road traffic, traffic lights, and other factors, the causes of the formation of the models can be determined. The results can be used as input to the BRT simulation system, so that the simulation is closer to the real system. And the main factors that have impact on the running state of hybrid BRT can be determined, this provides a basis for BRT optimization.

## 2. Modelling the interstation travel speed

Due to the influence of traffic lights, road traffic and other factors, the interstation speed distribution of hybrid BRT usually presents a multimodal phenomenon. The Gaussian mixture model can describe non-single normal samples, capture the heterogeneity of multiphase data more completely, and effectively fit the multimodal distribution. Therefore, this paper adopts a Gaussian mixture model to describe the interstation travel speed of hybrid BRT, and assumes the unknown parameters as random variables, and describes the speed model under the Bayesian framework.

### *2.1 The Gaussian mixture model*

A Gaussian mixture model is a simple weighted sum of K Gaussian densities, each representing a component that corresponds to a speed distribution in the proposed model. For any adjacent stations, the Gaussian mixture model of the travel speed is defined as Eq. (1)

$$p\left(y_i \mid \boldsymbol{\mu},\boldsymbol{\sigma}^2\right)=\sum_j^K w_j \cdot N\left(\mu_j,\sigma_j^2\right) \tag{1}$$

where $y_i$ is a target random variable representing the $i$ th travel speed extracted from bus station-reporting data, $p(|)$ is a composite probability density of travel speeds, $K$ is the component number in the model, $\boldsymbol{\mu}=\left(\mu_1,\cdots,\mu_K\right)'$ is a vector of speed mean of each component, and $\boldsymbol{\sigma}^2=\left(\sigma_1^2,\cdots,\sigma_K^2\right)'$ is a vector of speed variances of the components, $w_j$ is a weight of $j$ th component, $\sum_j^K w_j=1$ , and $N(\cdot,\cdot)$ is a one-dimensional Gaussian density function.

In the above model, the density distribution which the observed value $y_i$ belongs to is unknown. Define the latent variable $z_i$ as the density distribution label to which the observed value $y_i$ belongs, and the probability that the latent variable $z_i$ belongs to the $j$ th density distribution is as Eq. (2)

$$p\left(z_i=j\right)=w_j \text{ , } j=1,\cdots,K \tag{2}$$

Then a complete Gaussian mixture model of the interstation travel speed is parameterized by the number of the component and the mean, variance and weight for each component. However, the component number of the models and the parameters of each component are often variable among inter-stations. These differences are caused by the factors that have impact on the speed (such as road traffic lights). To model the travel speed better, this paper introduces the Bayesian framework, and uses the concept of hyper parameters to express the potential difference characteristics of the inter-station travel speed.

### *2.2 Travel speed model in Bayesian framework*

Under the Bayesian framework, the unknown parameters in the Gaussian mixture model are assumed to be random variables and to have their own certain prior distribution, and the posterior distribution of these parameters needs to be estimated. Regarding the conjugate priors of the parameters, the component number in the model was assumed to follow a Poisson distribution, the weight parameter was assumed to follow a symmetric Dirichlet distribution, the mean of travel speed for each density distribution was assumed to be normally distributed, the variance in travel speeds for each density distribution was assumed to follow an inverse Gamma distribution. All these prior distribution functions also involved additional parameters, which are referred to 'hyperparameter'. Eqs. (3)–(6) represent functional expressions for the chosen priors.

$$p\left(K=k\right)=\frac{\lambda^{k}\exp\left(-\lambda\right)}{k!} \tag{3}$$

$$\mathbf{w}\sim D\left(\delta,\cdots,\delta\right) \tag{4}$$

$$\mu_{j}\sim N\left(\xi,\kappa^{-1}\right),\ j=1,\cdots,K \tag{5}$$

$$\sigma_{j}\sim\Gamma\left(\alpha,\beta\right),\ j=1,\cdots,K \tag{6}$$

Where $\lambda$ is a hyperparameter to characterize the prior distribution of the number of the distributions, $D$ represents the Dirichlet distribution with a hyperparameter $\delta$ , $\xi$ and $\kappa^{-1}$ are the prior mean and variance of the prior distribution of the mean of the density distribution respectively, and $\Gamma\left(\cdot,\cdot\right)$ represents a Gamma distribution, and hyperparameters $\alpha$ and $\beta$ are shape and rate (i.e. 1/scale) parameters respectively.

The hyperparameters $\kappa$ and $\beta$ are defined as random parameters, as Eqs (7)-(8), otherwise if they are set to fixed values, the estimated number of density distributions will change with them, this will result in different values of $\kappa$ and $\beta$ for the travel speeds of different adjacent stations.

$$\kappa\sim\Gamma\left(e,f\right) \tag{7}$$

$$\beta\sim\Gamma\left(g,h\right) \tag{8}$$

where the second-level hyperparameters $e$ , $g$ and $f$ , $h$ represent the shape and rate of a Gamma density, respectively. According to the Bayesian theorem, the posterior distribution of all random variables can be defined as

$$\begin{aligned}
&p\left(\mathbf{w},\boldsymbol{\mu},\boldsymbol{\sigma}^{2},K,\mathbf{z},\kappa,\beta\mid\mathbf{y}\right)\propto p\left(\mathbf{y}\mid\mathbf{w},\boldsymbol{\mu},\boldsymbol{\sigma}^{2},K,\mathbf{z},\kappa,\beta\right)p\left(\mathbf{w},\boldsymbol{\mu},\boldsymbol{\sigma}^{2},K,\mathbf{z},\kappa,\beta\right)\\
&=p\left(\mathbf{y}\mid\boldsymbol{\mu},\boldsymbol{\sigma}^{2},\mathbf{z}\right)p\left(\boldsymbol{\mu}\mid\kappa,K\right)p\left(\boldsymbol{\sigma}^{2}\mid\beta,K\right)p\left(\mathbf{z}\mid\mathbf{w},K\right)p\left(\mathbf{w}\mid K\right)p\left(K\right)p\left(\kappa\right)p\left(\beta\right)\\
&=p\left(\mathbf{y}\mid\boldsymbol{\mu},\boldsymbol{\sigma}^{2},\mathbf{z}\right)p\left(\boldsymbol{\mu}\mid\xi,\kappa,K\right)p\left(\boldsymbol{\sigma}^{2}\mid\alpha,\beta,K\right)p\left(\mathbf{z}\mid\mathbf{w},K\right)p\left(\mathbf{w}\mid\delta,K\right)p\left(K\mid\lambda\right)p\left(\kappa\mid e,f\right)p\left(\beta\mid g,h\right)
\end{aligned} \tag{9}$$

Where $\mathbf{y}=\left(y_{1},\cdots,y_{N}\right)'$ and $\mathbf{z}=\left(z_{1},\cdots,z_{N}\right)'$ are observations and latent variable tags, Respectively, $N$ is the number of the observations. According to the conditions of the parameters independent assumptions, the posterior distribution can be simplified into one-level Bayesian model(second row of Eq.(9)), and further, can be simplified into the two-level Bayesian model in the third row of Eq.(9). In the next step, we need to solve the joint probability distribution of all the random variables in Eq. (9).

## 3. parameter estimation

After the interstation travel speed of hybrid BRT modelled, the component number and the parameters of each component need to be inferred, this inference process is also a process of solving the speed model. Because the model is a multimodal probability density distribution model, we use the outer Gibbs sampling and RJMCMC (Reversible-jump Markov chain Monte Carlo) method to solve it.

### *3.1 Gibbs sampler procedure*

To sample from a joint distribution, a Gibbs sampler repeatedly takes a draw of each random variable in turn, with all other variables fixed at the previous draws. It should be noted that the dimension of the first three parameter subsets vary according to the last parameter K. This was the main reason a reversible jump MCMC sampler was employed, the details of which will be described in the next subsection. The outer Gibbs sampler for solving the proposed problem can be summarized as follows.

1) to update the distribution shares $\mathbf{w}$ .
2) to update the mean $\boldsymbol{\mu}$ and variance $\boldsymbol{\sigma}^2$ of each distribution.
3) to update the latent allocation variable $\mathbf{z}$ for each travel speed.
4) to update the hyperparameters $\kappa$ and $\beta$ .
5) to update the number of speed components $K$ .

According to the conjugacy, all the conditional distribution in the first four steps can be achieved by simplifying the Eq. (9) with all other parameters fixed at constants.

The full conditional distribution for $\mathbf{w}$ parameter was a Dirichlet distribution with hyperparameters increased by the estimated number of observations (i.e. the number of travel speed observations) for each distribution.

$$\mathbf{w} \mid \textit{all other parameters} \sim D\left(\delta + n_1, \cdots, \delta + n_K\right) \tag{10}$$

The full conditional distribution of the mean of the speed density distribution is given in Eq. (11). To avoid the problem of label exchange between the distributions, we follow the order principle ( $\mu_1 < \mu_2 < \cdots < \mu_K$ ). during the procedure of speed mean sampling, once the order principle is violated, the sampling results are rejected.

$$\mu_j \mid \textit{all other parameters} \sim N\left\{ \frac{\sigma_j^{-2} \sum_{\{i \mid z_i = j\}} y_i + \kappa\xi}{\sigma_j^{-2} n_j + \kappa}, \left(\sigma_j^{-2} n_j + \kappa\right)^{-1} \right\} \tag{11}$$

The full conditional distribution of speed variance of the density distribution is given in Eq. (12).

$$\sigma_j^{-2} \sim \Gamma\left( \alpha + \frac{1}{2} n_j, \beta + \frac{1}{2} \sum_{\{i \mid z_i = j\}} \left(y_i - \mu_j\right)^2 \right) \tag{12}$$

The latent variable of the observed speed $y_i$ is sampled using Eq. (13).The estimated number of observed values is updated accordingly.

$$p\left(z_i = j \mid \textit{all other parameters}\right) \propto \frac{w_j}{\sigma_j} \exp\left\{ -\frac{\left(y_i - \mu_j\right)^2}{2\sigma_j^2} \right\} \tag{13}$$

The full conditional probability distribution of the hyperparameters $\kappa$ and $\beta$ are given in Eq. (14)-(15).

$$\kappa \mid \textit{all other parameters} \sim \Gamma\left\{ e + \frac{1}{2} K, f + \frac{1}{2} \sum_j \left(\mu_j - \xi\right)^2 \right\} \tag{14}$$

$$\beta \mid \textit{all other parameters} \sim \Gamma\left( g + K\alpha, h + \sum_j \sigma_j^{-2} \right) \tag{15}$$

In the fifth step, the RJMCMC method is used to realize the reversible jump of each parameter in different dimensions based on the four different move types of split, combine, birth and death, and to infer the unknown number of the components of the model.

### *3.2 Estimation of the number of speed component*

Based on the dimension equilibrium condition, the RJMCMC solves the mixture model under unknown dimension by exploring in different dimension spaces. The core of the RJMCMC algorithm is the accepted probability of a proposed move. Green (1995) suggested the following criterion [Eq. (16)] to move from the current state $x = \left(K, w_j, \mathbf{w}, \boldsymbol{\mu}, \boldsymbol{\sigma}^2, \mathbf{z}, \kappa, \beta\right)$ to a higher dimensional state $x' = \left(K + 1, \mathbf{w}, \boldsymbol{\mu}, \boldsymbol{\sigma}^2, \mathbf{z}, \kappa, \beta\right)$, as Eq. (16)-(18).

$$a_m\left(x, x'\right) = \min\left\{1, A\right\} \tag{16}$$

$$A = \left(\text{likelihood ratio}\right) \times \left(\text{prior ratio}\right) \times \left(\text{proposal ratio}\right) \times \left(\text{Jacobian}\right) \tag{17}$$

$$\text{likelihood ratio}=\frac{p\left(y\mid x'\right)}{p\left(y\mid x\right)},\ \text{prior ratio}=\frac{p\left(x'\right)}{p\left(x\right)},\ \text{proposal ratio}=\frac{r_m\left(x'\right)}{r_m\left(x\right)q\left(u\right)},\ \text{Jacobian}=\left|\frac{\partial x'}{\partial\left(x,u\right)}\right| \tag{18}$$

$r_m(x)$ is the proposal probability of selecting the movement type, $m$ in the current speed distribution $x$, $u$ is the continuous variable sample, and $q(u)$ is the proposal probability density distribution of $u$.

In each iteration, split or combine, birth, or death is selected according to the proposal probabilities of the movement type. $b_K$ is the proposal probability of splitting (or birth) when the current number of the speed density distributions is $K$, $d_K$ is the proposal probability of the corresponding combine (or death), as in Eq. (19). $K_{\max}$ is the maximum number of the speed distributions.

$$b_K=\begin{cases}1, K=1;\\0, K=K_{\max}\\0.5, \text{其它}.\end{cases},\quad d_K=\begin{cases}0, K=1;\\1, K=K_{\max}\\0.5, \text{其它}.\end{cases} \tag{19}$$

In case of the split move, the $j*$ distribution is randomly selected to be split. The weight, the mean and the variance of the speed of the distribution $j*$ are split into two new distributions $j1$ and $j2$, as in Eq.(20). And the observed values belonging to the distribution $j*$ are redistributed to the new distribution $j1$ or $j2$ using the Monte Carlo method, see Eq.(13). However, once the principle of order ( $\mu_{j*-1}<\mu_{j1}<\mu_{j2}<\mu_{j*+1}$ ) is violated, then the split will be rejected.

$$\begin{aligned}&u_1 \square\ beta\left(2,2\right), u_2 \square\ beta\left(2,2\right), u_3 \square\ beta\left(1,1\right)\\&w_{j1}=u_1 w_{j*},\ w_{j2}=\left(1-u_1\right)w_{j*}\\&\mu_{j1}=\mu_{j*}-u_2\sigma_{j*}\sqrt{\frac{w_{j2}}{w_{j1}}},\ \mu_{j2}=\mu_{j*}+u_2\sigma_{j*}\sqrt{\frac{w_{j1}}{w_{j2}}}\\&\sigma_{j1}^2=u_3\left(1-u_2^2\right)\sigma_{j*}^2\frac{w_{j*}}{w_{j1}},\ \sigma_{j2}^2=\left(1-u_3\right)\left(1-u_2^2\right)\sigma_{j*}^2\frac{w_{j*}}{w_{j2}}\end{aligned} \tag{20}$$

In case of combine move, the adjacent distributions $j1$ and $j2$ are merged into the distribution $j*$, as in Eq.(21).

$$\begin{aligned}&w_{j*}=w_{j1}+w_{j2}\\&w_{j*}\mu_{j*}=w_{j1}\mu_{j1}+w_{j2}\mu_{j2}\\&w_{j*}\left(\mu_{j*}^2+\sigma_{j*}^2\right)=w_{j1}\left(\mu_{j1}^2+\sigma_{j1}^2\right)+w_{j2}\left(\mu_{j2}^2+\sigma_{j2}^2\right)\end{aligned} \tag{21}$$

Then the acceptance probability of a split move can be defined as the minimum value between 1 and the result of Eq. (22). The probability of acceptance for a combine move is $\min\left\{1, A^{-1}\right\}$.

$$\begin{aligned}&\text{Likelihood ratio}=\frac{\left(\prod_{\{i|z_i=j1\}}N\left(y_i\mid\mu_{j1},\sigma_{j1}^2\right)\right)\left(\prod_{\{i|z_i=j2\}}N\left(y_i\mid\mu_{j2},\sigma_{j2}^2\right)\right)}{\prod_{\{i|z_i=j*\}}N\left(y_i\mid\mu_{j*},\sigma_{j*}^2\right)}\\&\text{Prior ratio}=\frac{p\left(K+1\right)}{p\left(K\right)}\times\left(K+1\right)\times\frac{w_{j1}^{\delta-1+n_{j1}}w_{j2}^{\delta-1+n_{j2}}}{w_{j*}^{\delta-1+n_{j1}+n_{j2}}B\left(\delta,K\delta\right)}\\&\times\sqrt{\frac{\kappa}{2\pi}}\exp\left[-\frac{1}{2}\kappa\left\{\left(\mu_{j1}-\xi\right)^2+\left(\mu_{j2}-\xi\right)^2-\left(\mu_{j*}-\xi\right)^2\right\}\right]\\&\times\frac{\beta^\alpha}{\Gamma\left(\alpha\right)}\left(\frac{\sigma_{j1}^2\sigma_{j2}^2}{\sigma_{j*}^2}\right)^{-\alpha-1}\exp\left\{-\beta\left(\sigma_{j1}^{-2}+\sigma_{j2}^{-2}-\sigma_{j*}^{-2}\right)\right\}\\&\text{Proposal ratio}=\frac{d_{K+1}}{b_K P_{alloc}}\left\{g_{2,2}\left(u_1\right)g_{2,2}\left(u_2\right)g_{1,1}\left(u_3\right)\right\}^{-1}\\&\text{Jacobian}=\frac{w_{j*}\left|\mu_{j1}-\mu_{j2}\right|\sigma_{j1}^2\sigma_{j2}^2}{u_2\left(1-u_2^2\right)u_3\left(1-u_3\right)\sigma_{j*}^2}\end{aligned} \tag{22}$$

Where $K$ is the number of the speed distributions before splitting, $n_{j1}$ and $n_{j2}$ are the number of observations assigned to the speed distributions $j1$ and $j2$, $B(\cdot,\cdot)$ is the beta function, $\Gamma(\cdot)$ is the gamma function, $P_{alloc}$ is the probability of occurrence of this particular allocation result, $g_{p,q}(\cdot)$ is the density function of the beta function with parameters $p$ and $q$.

When a birth move happens, a new speed distribution is generated, as Eq. (23), and the weight of all speed distributions is normalized.

$$w_{j*} \sim beta(1,K),\ \mu_{j*} \sim N(\xi,\kappa^{-1}),\ \sigma_j^{*} \sim \Gamma(\alpha,\beta) \tag{23}$$

The probability of acceptance for a birth move is $\min\{1,A\}$, see Eq.(24). The probability of acceptance for death move is $\min\{1,A^{-1}\}$. $K$ is the number of speed distributions before the birth move; $K_0$ is the number of empty speed distributions.

$$\begin{aligned}
&\text{Likelihood ratio=1}\\
&\text{Prior ratio=}\frac{p(K+1)}{p(K)}\times(K+1)\times\frac{w_{j*}^{\delta-1}}{B(\delta,K\delta)}(1-w_{j*})^{N+K\delta-K}\\
&\text{Proposal ratio=}\frac{d_{K+1}}{b_K K_0}g_{1,K}(w_{j*})^{-1}\\
&\text{Jacobian=}(1-w_{j*})^{K-1}
\end{aligned} \tag{24}$$

*3.3 Description of the running state of hybrid BRT*

The model above provide a method for descript the running state of hybrid BRT. Road traffic conditions are usually based on vehicle speed, the road is simply divided into smooth, slow, crowded, serious congestion and other states. BRT is the same. This simple state description can not effectively describe the speed distribution, the information provided is also very small. The Gaussian mixture model of interstation travel speed provides a new opportunity to describe the hybrid BRT running state. Each of the distributions of the model is treated as a sub-state, and the result of the whole model is the fusion of all sub-states, representing the interstation running state of the BRT. As the model provides a wealth of information, including the number of sub-states, the mean, variance and weight of each sub-state, etc., where the bigger number of sub-state, the more complex running state. So a comparative analysis can be performed between the results of different models and the corresponding interstation physical environment, and the causes leading to complex traffic conditions can be identified, this provide a base for optimizing hybrid BRT.

## 4. calibration and validation of the hyperparameters

The proposed model belongs to the category of unsupervised machine learning technologies that require no calibration. The calibration and validation here means the determination of hyperparameters that was included in the model to infer the original parameters for speed distributions within a Bayesian framework. The objective function of the model hyperparameter calibration is defined as the maximizing likelihood ratio of the Gaussian mixture model, as in Equation 25.

$$\max_{\boldsymbol{\theta}} \tilde{z}(\boldsymbol{\theta}) = \prod_{s}^{N_s}\left\{\rho_s \prod_{i}^{N} p(y_i \mid \boldsymbol{\mu},\boldsymbol{\sigma}^2)\right\} \tag{25}$$

Where $\tilde{z}(\cdot)$ is the objective function to be maximized, $\boldsymbol{\theta}$ is a vector of hyperparameters, è $=(\lambda,\delta,\xi,e,f,\alpha,g,h)$, $s$ is a link between neighbored stations of the mixed BRT, $N_s$ is the number of the links, $\rho_s$ is the weight of $s$.

Since $\tilde{z}(\cdot)$ was not a closed-form function, it could be evaluated by simulation. Furthermore, the function's mathematical properties such as continuity, differentiability, and concavity were totally unknown. It was thus impossible to employ a rigorous optimization algorithm like Newton–Raphson. The only way to optimize the objective function was to use metaheuristics. A particle-swarm optimization algorithm was the best fit for solving the above problem, since that algorithm is known to be good at optimizing a non-convex objective function with continuous variables.

The model calibration is done using the particle swarm optimization algorithm, the steps as follows:

1) to generate n particles, each particle randomly generates the initial solution,

2) to calculate the fitness function $z(\theta_i)$ ($i=1,\cdots,n$) of the current solution $\theta_i$ of each particle, as Eq. (26),

3) to obtain the optimal solution experienced by each particle, denoted as $\theta_{pi}$, and the optimal solution experienced by all particles, denoted as $\theta_g$,

4) to update current solution of the particles according to Eq. (26),

5) return to step 2 until the iteration finished.

$$\begin{aligned}&\mathbf{v}_i=\mathbf{v}_i+\mathbf{r}_1\cdot\left(\boldsymbol{\theta}_{pi}-\boldsymbol{\theta}_i\right)+\mathbf{r}_2\cdot\left(\boldsymbol{\theta}_g-\boldsymbol{\theta}_i\right)\\&\boldsymbol{\theta}_i=\boldsymbol{\theta}_i+\mathbf{v}_i\end{aligned} \tag{26}$$

Where $\boldsymbol{\theta}_i$ and $\mathbf{v}_i$ are the solution and corresponding speed of the particle $i$ respectively, $\mathbf{r}_1$ and $\mathbf{r}_2$ are random numbers with domain 0-1.

## 5. Case study

The case study is applied to Guangzhou Bus Rapid Transit (GBRT), a kind of hybrid BRT. Its corridor runs along the center line of Zhongshan Avenue, with a length of 23 kilometers. There are 26 stations, numbered 1 to 26, the first station is Tianhe Sports Center, the center of the downtown, the 26th is Xiayuan, located in the outskirts of the city (for details, see Appendix 1). Totally there are 31 bus lines, named from B1 to B31 respectively, but only B1 runs from the start BRT station to the end one, other bus lines only enter the BRT corridor in necessary, when they left the corridor, they are just ordinary bus lines. So, the ordinary bus lines do not separate from GBRT, and passengers can transfer in station. For this reason, GBRT is double efficient than other BRTs.

The station-reporting data of GBRT were collected at 7th Dec, 2015, and from them there are 65 thousand of the travel speed data of the inter-station (from Tianhe Sports Center to Xiayuan, totally 25 inter-stations,named by neighbored station numbers, as Figure 1) were computed (for detailed sample data, see Appendix 2) .

### *5.1 Calibration and validation results*

In the calibration process of the interstation travel speed model, the number of particles is set to 10, the number of iterations is set to 80 times. The hyperparameter $\lambda$ and $\delta$ set to 1, $\xi$ is set to the mean of the travel speed of corresponding inter-station, the calibration results as Table 1.

**Table 1** calibration values for hyperparameters.

| $\lambda$ | $\delta$ | $\xi$ | $e$ | $f$ | $\alpha$ | $g$ | $h$ |
|---|---|---|---|---|---|---|---|
| 1 | 1 | Midpoint value of $R$ | 1.71 | 5.07 | 2.30 | 2.75 | 8.37 |

*$R$ is the range of travel speeds data for each inter-station.

The RJMCMC method is applied to infer the number of speed distributions and the weight, mean and variance of each speed distribution, see Appendix 3. In the process, the adopted Gibbs sampler took random draws from the posterior distribution. After conducting 50,000 Gibbs iterations, the former 5000 replications were discarded as burn-in data, and the remaining draws were saved to approximate the joint posterior distribution of the parameters. Where the estimated number of the speed distributions was set as the number with the maximum marginal posterior probability, and a distribution's estimated travel speed was set as the mean of the marginal posterior distribution of the mean travel speed for the distribution. The estimated variance of travel speeds also denoted the mean of the posterior distribution for the variance in travel speeds of each distribution.

The results showed that the number of the speed distributions was different among the different inter-stations, it ranged from 1 to 6, and each number accounted for 8%, 44%, 16%, 16%, 12% and 4% of all the numbers, as in Figure 2. To illustrate the result, six estimated model of inter-station travel speed and corresponding histograms of observed speed samples were draw in Figure 1, their component number are from 1 to 6, respectively (for all results, see Appendix 3) . It could be found that the estimated results of the Bayesian prediction can be well fitted to the observed speed samples. It is difficult to visually judge the component number and the weight, speed mean and variance of each component according to the speed histogram, but in the estimated results they are vary clear, indicating that the proposed model is effective and necessary.

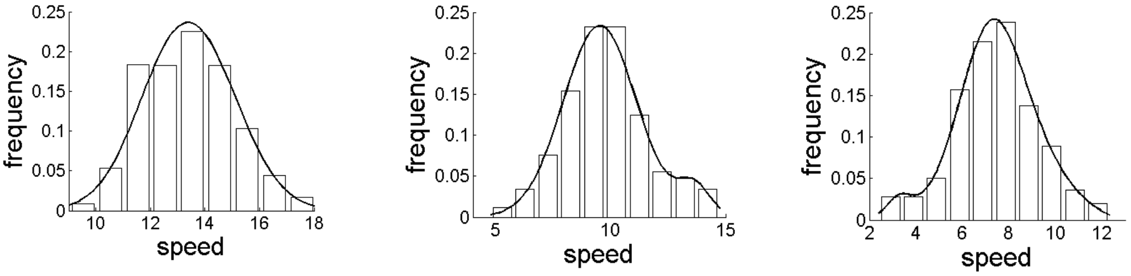

(a) $K=1$ Inter-station 16-17 (b) $K=2$ Inter-station 6-7 (c) $K=3$ Inter-station 3-4

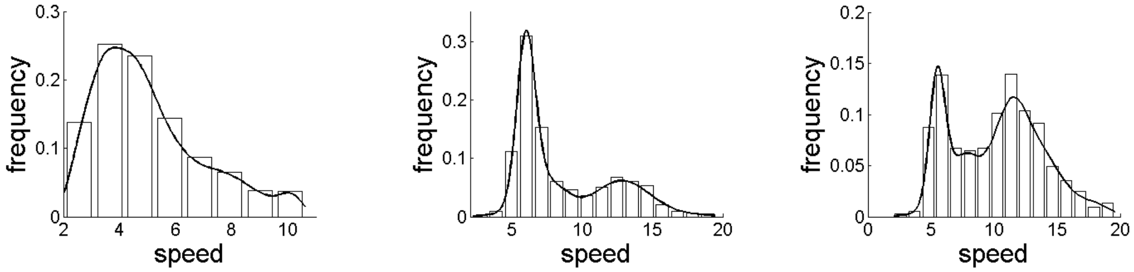

(d) $K=4$ Inter-station 1-2 (e) $K=5$ Inter-station 10-11 (f) $K=6$ Inter-station 9-10

**Figure 1.** Comparison of model curve of different interstation and corresponding histograms of speed samples

### *5.2 Running states of GBRT*

The modelling results shed a light on the running state of GBRT. If a component of Gaussian mixture model represents an interstation running state, then the model represents the mixture results of all the interstation running states. Figure 2 is the K values of all 25 interstations, the horizontal axis is the sequence of stations, the first station is Tianhe Sports Center, the 26th station is Xiayuan, and the 4th, 6th, 9th, 11th stations are Normal Univ & Jinan Univ, Shangshe, Tangdong, Chebei station respectively. Figure 3 is the posterior mean of the expected speed of the running states of all 25 interstations.

It can be observed from Figure 2, the K values of the models in urban area are higher than those in suburban. As the BRT part in suburban basically has no external disturbance, so we can conclude that the number of the running state of GBRT itself is 2. This conclusion can also be obtained from the urban section of GBRT, such as the inter-station of 6-7, from the GOOGLE map it can be seen, there are no road intersection and traffic lights, traffic is also not much, that is, there is no factor to interfere with BRT operation, so its K value is 2.

Also in the Figure 2, there are two sections with K value 5 or more. But combined with the GOOGLE map it can be found that the reasons are different. In the first part, there is a highway entrances between inter-station 4-5, which is a highway through the city center, and station 1 to 4 are work destinations, so the highway brings a lot of traffic flow, which disturbs GBRT a lot. The second part 9-11 crosses with main road (Chebei Road) plainly, this road is a north-south traffic arteries, connecting a fast road nearby, which brings a lot of traffic flow into the downtown, they disturb GBRT a lot, and the road has many straight traffic flow, so the buses of GBRT must wait for a long red time. so, the K value of inter-station 9-10, a maximum of 6, is the superimposed effect of the two factors.

On the other hand, the bigger K value of the interstation speed model means the more complex of the running state of the inter-station, this conclusion can be proved in Figure 3, it can be observed that posterior means of the means of the speeds are very scattered for those models with K value more than 4.

How to reduce the K value, that is, to reduce the complexity of the operating state of BRT? We can also find answer from GBRT. Comparing inter-station 10-11 and 7-8 (with K value 4) In the network map, they have similar environment. There is also a main road (Keyun Road) crossing with inter-station 7-8, a more important road than Chebei Road, but it passes through the inter-station below, thus the direct traffic flow interference is avoided, which greatly reduced the waiting time of GBRT buses for traffic lights. Inter-station 3-4 is in a similar situation, but the solution is to raise the BRT lane through the intersection, thus avoiding the disturbance of traffic lights and other directions of traffic.

Therefore, the main road traffic flow and traffic lights are the main factors affecting the BRT running state, the solution is to elevate BRT lane, or let other main road cross through the BRT lane below, if the traffic flow of the main road is relatively large.

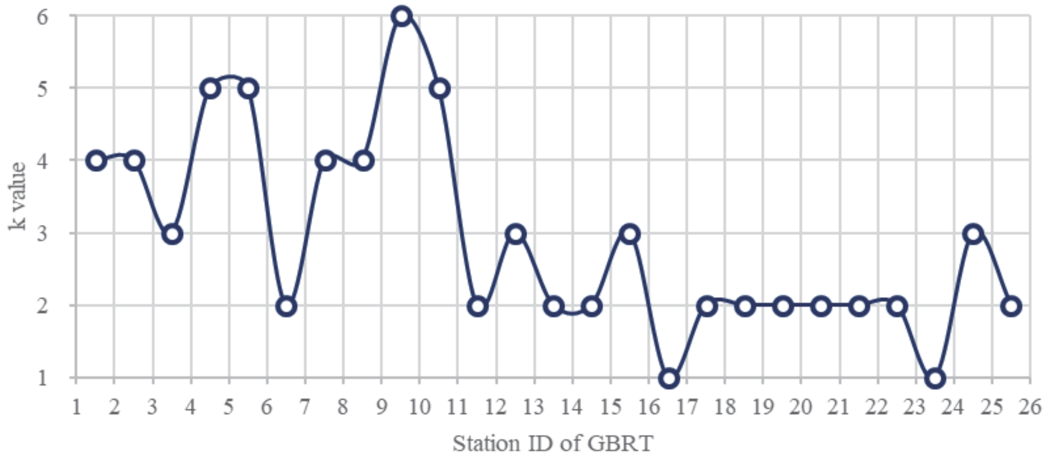

**Figure 2.** $K$ values of the interstation travel speed models.

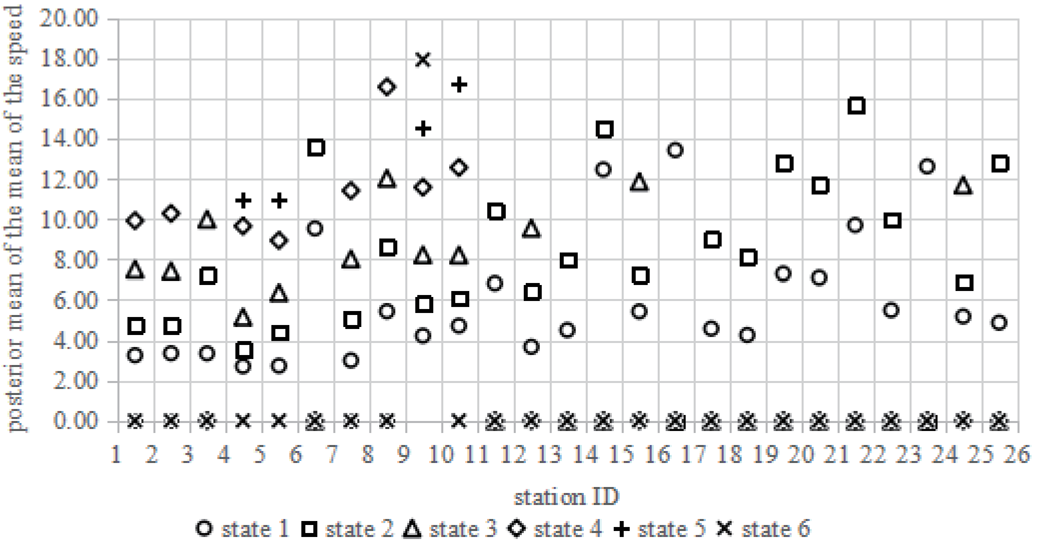

**Figure 3.** Estimated speed of the interstation travel states of GBRT

## Conclusions

Hybrid BRT greatly improves the operational efficiency of urban public transport, but it is also disturbed by urban road traffic. Due to road traffic, traffic lights and other factors, the distribution and changes of its interstation travel speed are very complex. In this paper, a Gaussian mixture model describing the interstation travel speed of hybrid BRT under Bayesian framework is established. The component number of of the model and the weight, mean and variance of each component are deduced by RJMCMC method. The model is applied to the Guangzhou BRT, and the travel speed of 25 inter-stations is modeled to describe their running states. It can be observed that the model can very effectively describe the heterogeneous speed data among different inter-stations, and provide richer information usually not available from the traditional models. The causes of different speed distribution can also be identified, this provides a base for optimizing hybrid BRT.

Firstly, the component number of different speed model varied greatly, the value is from 1 to 6, this implies the proposed model is necessary and appropriate.

Second, the number of the running state is usually 2 for GBRT itself, but as the influencing factors increase, the number increases consequently, until to 6.

Third, the main road will lead to many traffic and long time to wait for the red light, they will have a serious impact on the running state if it crosses with the BRT. The way to reduce these effects is to elevate the BRT lane through the main road, or to sink the road through the BRT lane.

## Acknowledgements

The authors acknowledge that this paper was prepared based on Science and technology planning project of Guangdong province of China in 2017 (No. 2017B010111007),the National Natural Science 16 Foundation of China (No. 41271181).

## Appendix

Appendix 1 the stations of GBRT (the station name is mainly named in Chinese pinyin)

| Station ID | Station Name | Station ID | Station Name | Station ID | Station Name |
|---|---|---|---|---|---|
| 1 | Tianhe Sports Center | 10 | Tianlang mingju | 19 | Wuchong |
| 2 | Shipai Qiao | 11 | Chebei | 20 | Huangpu Coach Station |
| 3 | Gangding | 12 | Dongpuzhen | 21 | Shuanggang |
| 4 | Normal Univ & Jinan Univ | 13 | Huangcun | 22 | Shapu |
| 5 | Huajing New Town | 14 | Zhucun | 23 | Nanhai Temple |
| 6 | Shangshe | 15 | Lianxi | 24 | Miaotou |
| 7 | Xueyuan | 16 | Maogang | 25 | Nanwan |
| 8 | Xueyuan | 17 | Zhujiangcun | 26 | Xiayuan |
| 9 | Tangdong | 18 | Xiasha | | |

Appendix 2 The samples of the station-reporting data( the data is collected from bus801189, line B1)

| Line name | Bus number | Station | Reporting time | Tags of in/out |
|---|---|---|---|---|
| Line B1 | 801189 | Tianhe Sports Center | 2015-12-7 11:00:20 | Out |
| Line B1 | 801189 | Shipai Qiao | 2015-12-7 11:02:27 | In |
| Line B1 | 801189 | Shipai Qiao | 2015-12-7 11:02:40 | Out |
| Line B1 | 801189 | Gangding | 2015-12-7 11:06:13 | In |
| Line B1 | 801189 | Gangding | 2015-12-7 11:06:55 | Out |
| Line B1 | 801189 | Normal Univ & Jinan Univ | 2015-12-7 11:08:43 | In |
| Line B1 | 801189 | Normal Univ & Jinan Univ | 2015-12-7 11:09:21 | Out |
| Line B1 | 801189 | Huajing New Town | 2015-12-7 11:11:01 | In |
| Line B1 | 801189 | Huajing New Town | 2015-12-7 11:11:48 | Out |
| Line B1 | 801189 | Shangshe | 2015-12-7 11:12:56 | In |
| Line B1 | 801189 | Shangshe | 2015-12-7 11:13:20 | Out |
| Line B1 | 801189 | Xueyuan | 2015-12-7 11:14:08 | In |
| Line B1 | 801189 | Xueyuan | 2015-12-7 11:14:31 | Out |
| Line B1 | 801189 | Tangxiacun | 2015-12-7 11:16:59 | In |
| Line B1 | 801189 | Tangxiacun | 2015-12-7 11:17:29 | Out |
| Line B1 | 801189 | Tangdong | 2015-12-7 11:18:06 | In |
| Line B1 | 801189 | Tangdong | 2015-12-7 11:18:29 | Out |
| Line B1 | 801189 | Tianlangmingju | 2015-12-7 11:19:05 | In |
| Line B1 | 801189 | Tianlangmingju | 2015-12-7 11:19:30 | Out |
| Line B1 | 801189 | Chebei | 2015-12-7 11:20:15 | In |
| Line B1 | 801189 | Chebei | 2015-12-7 11:20:44 | Out |
| Line B1 | 801189 | Dongpuzhen | 2015-12-7 11:22:11 | In |
| Line B1 | 801189 | Dongpuzhen | 2015-12-7 11:22:40 | Out |
| Line B1 | 801189 | Huangcun | 2015-12-7 11:24:10 | In |
| Line B1 | 801189 | Huangcun | 2015-12-7 11:24:33 | Out |
| Line B1 | 801189 | Zhucun | 2015-12-7 11:26:26 | In |
| Line B1 | 801189 | Zhucun | 2015-12-7 11:26:58 | Out |

| Line name | Bus number | Station | Reporting time | Tags of in/out |
|---|---|---|---|---|
| Line B1 | 801189 | Lianxi | 2015-12-7 11:28:37 | In |
| Line B1 | 801189 | Lianxi | 2015-12-7 11:29:03 | Out |
| Line B1 | 801189 | Maogang | 2015-12-7 11:29:53 | In |
| Line B1 | 801189 | Maogang | 2015-12-7 11:30:18 | Out |
| Line B1 | 801189 | Zhujiangcun | 2015-12-7 11:32:06 | In |
| Line B1 | 801189 | Zhujiangcun | 2015-12-7 11:32:40 | Out |
| Line B1 | 801189 | Xiasha | 2015-12-7 11:34:48 | In |
| Line B1 | 801189 | Xiasha | 2015-12-7 11:35:18 | Out |
| Line B1 | 801189 | Wuchong | 2015-12-7 11:38:18 | In |
| Line B1 | 801189 | Wuchong | 2015-12-7 11:39:01 | Out |
| Line B1 | 801189 | Huangpu Coach Station | 2015-12-7 12:17:10 | In |
| Line B1 | 801189 | Huangpu Coach Station | 2015-12-7 12:17:22 | Out |
| Line B1 | 801189 | Shuanggang | 2015-12-7 12:21:59 | In |
| Line B1 | 801189 | Shuanggang | 2015-12-7 12:22:11 | Out |
| Line B1 | 801189 | Shapu | 2015-12-7 12:23:20 | In |
| Line B1 | 801189 | Shapu | 2015-12-7 12:23:32 | Out |
| Line B1 | 801189 | Nanhai Temple | 2015-12-7 12:24:30 | In |
| Line B1 | 801189 | Nanhai Temple | 2015-12-7 12:24:42 | Out |
| Line B1 | 801189 | Miaotou | 2015-12-7 12:25:32 | In |
| Line B1 | 801189 | Miaotou | 2015-12-7 12:25:44 | Out |
| Line B1 | 801189 | Nanwan | 2015-12-7 12:27:14 | In |
| Line B1 | 801189 | Nanwan | 2015-12-7 12:27:26 | Out |
| Line B1 | 801189 | Xiayuan | 2015-12-7 12:28:07 | In |

* interstation travel speed=interstation lane length/ (in time of current station- out time of previous station)

## Appendix 3 the Estimated Values of the Interstation Models of GBRT

| Interstation ID | Component number | Parameter values of each component | | | | | | |
|---|---|---|---|---|---|---|---|---|
| | | Parameter | 1 | 2 | 3 | 4 | 5 | 6 |
| 1-2 | 4 | mean | 3.2510 | 4.7673 | 7.5052 | 9.9131 | - | |
| | | variance | 0.6567 | 0.9772 | 1.0540 | 0.5350 | | |
| | | weight | 0.2844 | 0.4902 | 0.1824 | 0.0430 | | |
| 2-3 | 4 | mean | 3.3493 | 4.7628 | 7.4201 | 10.2722 | - | |
| | | variance | 0.5114 | 0.9080 | 1.0799 | 1.3580 | | |
| | | weight | 0.3122 | 0.3154 | 0.2699 | 0.1025 | | |
| 3-4 | 3 | mean | 3.3452 | 7.2113 | 9.9850 | - | | |
| | | variance | 0.5656 | 1.3406 | 1.1374 | | | |
| | | weight | 0.0463 | 0.7962 | 0.1575 | | | |
| 4-5 | 5 | mean | 2.7049 | 3.5278 | 5.1521 | 9.6434 | 10.9758 | - |
| | | variance | 0.3050 | 0.4935 | 0.7621 | 1.7421 | 1.1170 | |
| | | weight | 0.1003 | 0.0508 | 0.0555 | 0.4741 | 0.3193 | |
| 5-6 | 5 | mean | 2.7290 | 4.4130 | 6.3569 | 8.9291 | 10.9554 | - |
| | | variance | 0.3795 | 0.7524 | 0.9311 | 0.9566 | 0.6042 | |
| | | weight | 0.1575 | 0.4369 | 0.2276 | 0.1341 | 0.0440 | |
| 6-7 | 2 | mean | 9.5269 | 13.5904 | - | | | |
| | | variance | 1.5936 | 0.6886 | | | | |
| | | weight | 0.9321 | 0.0679 | | | | |
| 7-8 | 4 | mean | 2.9951 | 5.0860 | 8.0131 | 11.4071 | - | |
| | | variance | 0.5521 | 1.1308 | 1.3667 | 0.6810 | | |
| | | weight | 0.1251 | 0.5669 | 0.2622 | 0.0458 | | |

| Interstation ID | Component number | Parameter values of each component | | | | | | |
|---|---|---|---|---|---|---|---|---|
| | | Parameter | 1 | 2 | 3 | 4 | 5 | 6 |
| 8-9 | 4 | mean | 5.4349 | 8.6181 | 12.0195 | 16.5638 | - | |
| | | variance | 0.7542 | 1.7467 | 1.5425 | 1.3547 | | |
| | | weight | 0.2134 | 0.4307 | 0.3363 | 0.0195 | | |
| 9-10 | 6 | mean | 4.2223 | 5.8194 | 8.2147 | 11.5758 | 14.4941 | 17.9123 |
| | | variance | 1.0963 | 0.8013 | 1.1026 | 1.3448 | 1.3659 | 1.1198 |
| | | weight | 0.0335 | 0.2247 | 0.1761 | 0.3588 | 0.1672 | 0.0397 |
| 10-11 | 5 | mean | 4.7181 | 6.0802 | 8.2034 | 12.5544 | 16.7726 | - |
| | | variance | 1.2262 | 0.7513 | 1.1629 | 1.7347 | 1.5659 | |
| | | weight | 0.0490 | 0.4864 | 0.1537 | 0.2621 | 0.0488 | |
| 11-12 | 2 | mean | 6.8155 | 10.4426 | - | | | |
| | | variance | 1.1517 | 1.7286 | | | | |
| | | weight | 0.5239 | 0.4761 | | | | |
| 12-13 | 3 | mean | 3.6690 | 6.4205 | 9.5419 | - | | |
| | | variance | 0.7143 | 1.3528 | 1.5391 | | | |
| | | weight | 0.1366 | 0.5548 | 0.3086 | | | |
| 13-14 | 2 | mean | 4.5022 | 7.9813 | - | | | |
| | | variance | 0.7519 | 2.1595 | | | | |
| | | weight | 0.3546 | 0.6454 | | | | |
| 14-15 | 2 | mean | 12.4571 | 14.5260 | - | | | |
| | | variance | 1.1832 | 1.4558 | | | | |
| | | weight | 0.6132 | 0.3868 | | | | |
| 15-16 | 3 | mean | 5.4279 | 7.2572 | 11.8534 | - | | |
| | | variance | 0.5403 | 1.2110 | 1.9680 | | | |
| | | weight | 0.2231 | 0.3172 | 0.4598 | | | |
| 16-17 | 1 | mean | 13.4194 | - | | | | |
| | | variance | 1.6674 | | | | | |
| | | weight | 1.0000 | | | | | |
| 17-18 | 2 | mean | 4.5750 | 9.0009 | - | | | |
| | | variance | 1.2792 | 2.2615 | | | | |
| | | weight | 0.4637 | 0.5363 | | | | |
| 18-19 | 2 | mean | 4.2578 | 8.1231 | - | | | |
| | | variance | 0.8942 | 1.4810 | | | | |
| | | weight | 0.6028 | 0.3972 | | | | |
| 19-20 | 2 | mean | 7.2892 | 12.8186 | - | | | |
| | | variance | 1.9520 | 1.5421 | | | | |
| | | weight | 0.6603 | 0.3397 | | | | |
| 20-21 | 2 | mean | 7.0950 | 11.6966 | - | | | |
| | | variance | 1.2979 | 1.7037 | | | | |
| | | weight | 0.6196 | 0.3804 | | | | |
| 21-22 | 2 | mean | 9.6947 | 15.6545 | - | | | |
| | | variance | 2.0056 | 1.2307 | | | | |
| | | weight | 0.8620 | 0.1380 | | | | |
| 22-23 | 2 | mean | 5.4889 | 9.9591 | - | | | |
| | | variance | 0.6875 | 1.6440 | | | | |
| | | weight | 0.1051 | 0.8949 | | | | |
| 23-24 | 1 | mean | 12.6109 | - | | | | |
| | | variance | 2.4286 | | | | | |
| | | weight | 1.0000 | | | | | |
| 24-25 | 3 | mean | 5.1802 | 6.8780 | 11.6853 | - | | |
| | | variance | 0.4809 | 1.0225 | 2.0139 | | | |
| | | weight | 0.4070 | 0.3084 | 0.2846 | | | |

| Interstation ID | Component number | Parameter values of each component | | | | | | |
|---|---|---|---|---|---|---|---|---|
| | | Parameter | 1 | 2 | 3 | 4 | 5 | 6 |
| 25-26 | 2 | mean | 4.8721 | 12.8046 | - | | | |
| | | variance | 1.1996 | 3.2176 | | | | |
| | | weight | 0.1105 | 0.8895 | | | | |

## References

[1] DENG T.T., and John D. NELSON. Recent Developments in Bus Rapid Transit: A Review of the Literature. Transport Reviews, Vol. 31, No. 1, January 2011, pp. 69–96.

[2] Park B. J., and Zhang Y., and Lord D. Bayesian mixture modeling approach to account for heterogeneity in speed data[J]. Transportation research part B: methodological, Vol. 44, No 5, 2010, pp. 662-673.

[3] McLean, J. R. Observed speed distributions and rural road traffic operations. Proceedings of the 9th Australian Road Research Board Conference, Part 5, Australian Road Research Board, Vermont South, Victoria, Australia, 1978, pp. 235-244.

[4] Dey, P. P, Chandra, C., Gangopadhaya, S. Speed distribution curves under mixed traffic conditions. Journal of Transportation Engineering.Vol. 132, No. 6, 2006, pp. 475-481.

[5] Ko, J., Guensler, R. L. Characterization of congestion based on speed distribution: a statistical approach using Gaussian mixture model, TRB 2005 Annual Meeting CD-ROM, 2005.

[6] Jun, J. Understanding the variability of speed distributions under mixed traffic conditions caused by holiday traffic. Transport Research. Part C: Emergent Technology, Vol. 18, No.4, 2010, pp. 599–610.

[7] Corey, J., Lao, Y., Wu, Y.J., Wang, Y.,. Detection and correction of inductive loop detector sensitivity errors by using gaussian mixture models. Transportation Research Record: Journal of the Transportation Research Board, Vol. 2256, No. 1, 2011, pp. 120–129.

[8] Lao, Y., Zhang, G., Corey, J., Wang, Y. Gaussian mixture model-based speed estimation and vehicle classification using single-loop measurements. Journal of Transportation System, Vol. 16 No. 4, 2012, pp. 184–196.

[9] Richardson, S., Green, P.J. On Bayesian analysis of mixture models with an unknown number of components (with discussion). Journal of The Royal Statistical Society, Ser. B59, 1997, pp. 731–792.

[10] Green, P.J. Reversible jump Markov chain Monte Carlo computation and Bayesian model determination. Biometrika, 82 (4), 1995, pp. 711–732.

[11] Lee M., Sohn K. Inferring the route-use patterns of metro passengers based only on travel-time data within a Bayesian framework using a reversible-jump Markov chain Monte Carlo (MCMC) simulation. Transportation Research Part B, Vol. 81, 2015, pp. 1–17.

# Sensitivity Analysis and Selection of Check Index of Signal Intersection Simulation Model Based on VISSIM

**Mengda Zhang[1], Chenjing Zhou[2], Tian-tian Zhang[3], Yan Han[4*]**

1 Beijing Engineering Research Center of Urban Transport Operation Guarantee, Beijing University of Technology, China, No.100 Pingleyuan, Chaoyang District, Beijing
2 School of Civil and Transportation Engineering, Beijing University of Civil Engineering and Architecture, China, No.15 Yongyuan street, Daxing District, Beijing
3 Beijing Engineering Research Center of Urban Transport Operation Guarantee, Beijing University of Technology, China, No.100 Pingleyuan, Chaoyang District, Beijing
4 Beijing Engineering Research Center of Urban Transport Operation Guarantee, Beijing University of Technology, China, No.100 Pingleyuan, Chaoyang District, Beijing

*Corresponding Author:Yan Han, Beijing Engineering Research Center of Urban Transport Operation Guarantee, Beijing University of Technology, China, No.100 Pingle*yuan, Chaoyang District, Beijing*

## Abstract

Selecting check index quantitatively is the core of the calibration of micro traffic simulation parameters at signal intersection. Five indexes in the node (intersection) module of VISSIM were selected as the check index set. Twelve simulation parameters in the core module were selected as the simulation parameters set. Optimal process of parameter calibration was proposed and model of the intersection of Huangcun west street and Xinghua street in Beijing was built in VISSIM to verify it. The sensitivity analysis between each check index and simulation parameter in their own set was conducted respectively. Sensitive parameter sets of different check indices were obtained and compared. The results show that different indexes have different size of set, and average vehicle delay's is maximum, so it's necessary to select index quantitatively. The results can provide references for scientific selection of the check indexes and improve the study efficiency of parameter calibration.

**Keywords:** *micro traffic simulation; signal intersection; check index; sensitivity analysis; VISSIM*

## 1. Introduction

Microscopic traffic simulation is one of the most important tools for traffic design, planning and analysis. Before the simulation experiment is carried out, the simulation parameters need to be calibrated to improve the accuracy of the model. It can also guarantee that the program evaluation using simulation model have more referential value. The basic calibration process of the micro-simulation model includes four steps: selecting the check index, measuring road data, designing the simulation experiment and obtaining the parameter scheme in which the index error between the road measurement and simulation is minimum by adjusting the parameters. Selecting the check index quantitatively is the core of the parameter calibration. Recent studies lacks scientific and quantized selection methods of check indexes which cannot guarantee the validity of selecting the check indexes and greatly decreased solution efficiency. Therefore, it is necessary to reasonably select and calibrate the check indexes to improve the calibration accuracy of the micro-simulation model.

The rest of the paper is organized as follows. The second part shows the process of micro-traffic parameter calibration and the selection of indexes on related research, analyzes the shortcomings of these process and proposes the improvement ideas of them. The third part establishes a sensitivity analysis model based on variance and proposed the basis of sensitivity judgment. The fourth part collects the actual data from intersection of Huangcun West Street and Xinhua Street. VISSIM was used to establish the road network model. The final data summary of the whole experiment is displayed in this part. The last part summarizes the full text.

## 2. Literature Review

The parameter calibration was generally proceeded according to the flow in Figure 1. As the intelligent algorithm matured and was introduced into the traffic simulation field, the workflow changed from Figure 1 to Figure 2. The core idea remained unchanged, but the number of iterations and the calculation accuracy of the model was improved.

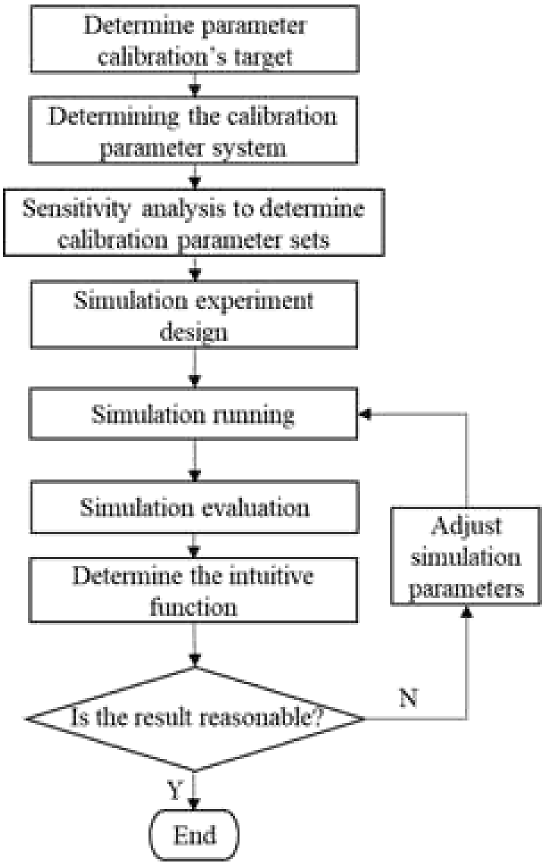

**Figure 1.** Calibration Process of Experimental Design Parameters

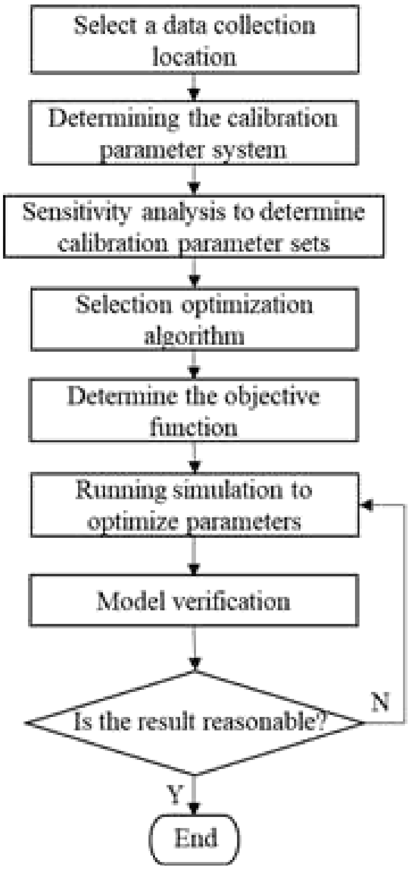

**Figure 2** Calibration Process of Intelligent Algorithm Parameters

It can be seen that the step "sensitivity analysis to determine the calibration parameter sets" in both two workflows require a pre-step which is determining the check index. But the researchers often determined the check index based on empirical judgments or qualitative analyses. Li Zhenlong used the average delay deviation of the entrance lane as the check index (Li Zhenlong et al., 2015). Nurlan Muhan chose queue length and travel time as the check indexes for VISSIM simulation model parameter calibration (Nurlan Muhan, 2014). Li Yan analyzed all check indexes qualitatively and selected travel time and maximum queue length as the check indexes (Li Yan, 2014). Xu Yuexin selected the intersection delay, parking delay, as the check index (Xu Yuexin et al., 2015).

In summary, recent studies lacks scientific and quantized selection methods of check indexes which cannot guarantee the validity of selecting the check indexes. Whether the determined check indexes are optimal or not remains to be discussed. Therefore, the sensitivity analysis method based on the variance analysis was proposed to select the optimal check index.

## 3. Establishment of Sensitivity Analysis Method Based on The Variance Analysis

### *3.1 Optimization Parameter Calibration Process Establishment*

In order to select the check index quantitatively, it is necessary to optimize the parameter calibration process. The optimized micro-simulation model parameter calibration flow is shown as Figure 3.

For improving the accuracy and work efficiency, it is necessary to analyze the parameter sensitivity based on the variance analysis. According to the analysis result, the optimal check index and the calibration parameters set are determined. And then the actual data is collected, the optimization algorithm is selected to establish the objective function. The parameters are optimized by running simulation and finally the model is verified.

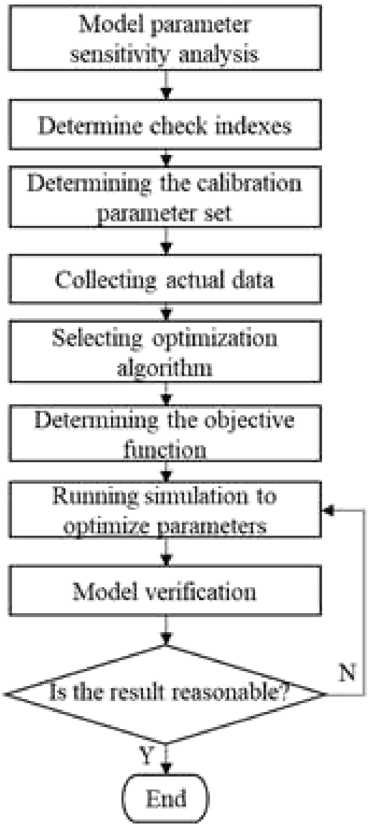

**Figure 3** Optimized Process of Micro-Simulation Model Parameter Calibration

### *3.2 Sensitivity Analysis Method Based on Variance Analysis*

The sensitivity analysis method of the model based on the variance analysis is the premise of determining the optimal check index. It is a key step of the parameter calibration optimal process of the micro-simulation model.

The sensitivity analysis method is based on the optimized variance analysis (Zhou Chenjing et al., 2016). The analysis idea is to compare the check indexes' variation changes caused by the simulation parameters with that by the stochastic parameters. The sensitivity relationship between simulation parameters and check indexes are judged. And it is shown as equations (1) - (4):

$$M_{AB} = \begin{vmatrix} x_{11} & \cdots & x_{1n} \\ \vdots & \ddots & \vdots \\ x_{m1} & \cdots & x_{mn} \end{vmatrix} \tag{1}$$

$$I = \frac{\sum_i^X \mathrm{STDEVA}(x_{i1}, x_{i2}, \cdots, x_{in})}{} \tag{2}$$

$$I' = \frac{\sum_j^Y \mathrm{STDEVA}(x_{1j}, x_{2j}, \cdots, x_{mj})}{} \tag{3}$$

$$P = \frac{\mathrm{I}}{I'} \tag{4}$$

Where: $M_{AB}$ is the result matrix of the simulation parameter A and the check index B, and i=1，2，3，……，X is the parameter value level of simulation parameters, and j=1，2，3，……，Y is the parameter value level of random seed, and I is the arithmetic mean value of the standard deviation of the change of the check index value caused by the change of the simulation parameter value, and $I'$ the arithmetic mean value of the standard deviation of the change of the check index value caused by the change of the random seed value, and STDEVA（$x_i$）is a function that finds the standard deviation of $x_i$, and P is check indicator to judge whether the simulation parameter is sensitive to the check index or not. When P is less than 1, it is considered that this simulation parameter is not sensitive to this check index, not so sensitive when P is between 1 and 1.5, the simulation parameter is not so sensitive to the check index. When P is greater than 1, the simulation parameter is sensitive to the check index.

## 4. VISSIM Simulation Model for Signalized Intersections

### *4.1 Selection of Check Index Set*

A number of check indexes are provided by VISSIM as shown in Table 1. Those check indexes are divided into three sections according to the evaluation object such as road, node (intersection) and road network. Considering that node (intersection) is usually used to describe the signalized intersection, five indexes in the node (intersection) module such as traffic flow, average delay, travel time, number of stops and queue length are selected as the experimental check index set.

**Table 1** Check Indexes

| Evaluation object | Check Index |
|---|---|
| Road | Density |
| | Average speed |
| | Traffic flow |
| | Lost time |
| Node (intersection) | Traffic flow |
| | Average delay |
| | Travel time |
| | Number of stops |
| | Queue length (maximum, average) |
| Road network | Number of vehicles leaving the road network |
| | Number of vehicles entering the road network |
| | Total path distance |
| | Total travel time |
| | Average speed |
| | Parking delay |
| | Number of stops |
| | Total number of parks |

### *4.2 Parameter Set Selection and Parameter Value Level Setting*

Twelve simulation parameters such as maximum forward distance and maximum deceleration in the vehicle following behavior module and lane change behavior module in VISSIM are selected as the parameter set. In order to conduct the sensitivity analysis, it is necessary to set the parameter value level of both the random seed and each simulation parameter.

The greater the number of levels, the closer the sensitivity of the simulation and that of the reality is. Considering the factors such as workload, time and researcher's ability, five levels are set for each parameter including random seed. The parameter value level, which is marked with *, is the default value of the corresponding simulation parameter. All parameter value levels change with equal difference or ratio based on their default values and are kept within their order of magnitude as far as possible. In summary, the simulation parameter levels are shown in Table 2.

**Table 2** Parameter Value Levels of Parameter in Set

| Module | Parameter | Default | Unit | Level 1 | Level 2 | Level 3 | Level 4 | Level 5 |
|---|---|---|---|---|---|---|---|---|
| Vehicle following behavior | Maximum forward distance | 0~250 | m | 0~150 | 0~200 | *0~250 | 0~300 | 0~350 |
| | Number of vehicles observed | 2 | veh | 1 | *2 | 3 | 4 | 5 |
| | Average parking distance | 2 | m | 0.5 | 1 | *2 | 4 | 8 |
| | Additional part of the safety distance | 2 | | 0.25 | 0.5 | 1 | *2 | 4 |
| | Multiple of the safety distance | 3 | | 0.75 | 1.5 | *3 | 6 | 12 |

| Module | Parameter | Default | | Unit | Level 1 | Level 2 | Level 3 | Level 4 | Level 5 |
|---|---|---|---|---|---|---|---|---|---|
| Lane change behavior | Maximum deceleration | -4 | -3 (rear car) | $m/s^2$ | *-4; -3 | -4; -2 | -4; -1 | -3; -1 | -3; -2 |
| | Acceptable deceleration | -1 | -1 (rear car) | $m/s^2$ | *-1;-1 | -1.5; | -2; -2 | -2.5; | -3; -3 |
| | $-1m/s^2$ | 100 | 100 (rear car) | | 50; 50 | *100; 100 | 150; 150 | 200; 200 | 250; 250 |
| | Waiting time before disappearing | 60 | | s | 15 | 30 | *60 | 120 | 240 |
| | Minimum headway distance | 0.5 | | m | 0.1 | 0.3 | *0.5 | 0.7 | 0.9 |
| | Safety distance conversion factor | 0.6 | | | 0.2 | 0.4 | *0.6 | 0.8 | 1 |
| | Maximum deceleration of combined braking | -3 | | $m/s^2$ | -1 | -2 | *-3 | -4 | -5 |
| Other simulation parameters | Random seed | 42 | | | 10 | 20 | 40 | 80 | 160 |

## 5. Case study

### *5.1 Data Acquisition*

The intersection of Huangcun West Street and Xinghua Street is formed by a trunk road and a secondary road. The entrance lanes are complete and typical. Seen from the signal timing scheme, this intersection uses a typical four-phase (four phases are north-south straight, north-south turn, east-west straight and east-west turn). Its transportation is convenient for on-site investigations repeatedly, so it is selected to provide actual data for model establishment in VISSIM. The lanes composition and road size data of each entrance and exit are shown in Table 3.

**Table 3** Lanes Composition and Road Size

| | Lanes composition | | | lane width /m | length of extension section/m | length of gradient section/m |
|---|---|---|---|---|---|---|
| | Left turn | Straight | Right turn | | | |
| East entrance | 1 | 2 | 1 | 3.5 | 51.8 | 20.3 |
| East exit | | | | 3.5 | 52.5 | 16.1 |
| South entrance | 1 | 3 | 1 | 3.5 | 68.6 | 7.7 |
| South exit | | | | 3.5 | 0 | 0 |
| West entrance | 1 | 2 | 1 | 3.5 | 42.7 | 21 |
| West exit | | | | 3.5 | 43.4 | 23.1 |
| North entrance | 2 | 3 | 1 | 3.5 | 84 | 9.1 |
| North exit | | | | 3.5 | 0 | 0 |

### *5.2 VISSIM Modeling and Experiment Conducting*

Using the actual data above, the road network is established in VISSIM. According to the calculation method of the traffic intersection capacity specified in Code for Planning of Intersections on Urban Roads, the traffic capacity of each entrance is calculated——Southern entrance: 3,731veh, North entrance: 3,992veh, West entrance: 2,417veh, and East entrance: 2,417veh. The driving path decision is set according to the actual running rules, and finally the detectors on the road are set up to complete the VISSIM model.

The goal of experiment is to prove that the sizes of the sensitive simulation parameter sets of different check indexes are different. The simulation parameters corresponding to each level value of random seed are put into VISSIM for simulation. Stop the experiment when all the results data are finally got.

### *5.3 Data Calculation*

Four detectors such as data collector, travel time detector, queue length counter and delay are provided for users in VISSIM. The output detection data are collected and the result matrixes of the simulation parameters and the check indexes are obtained. The result matrix of $-1m/s^2$ and the flow is as an example shown in the Table 4. According to formula (3), the P value of the matrixes can be obtained, and the sensitivity can be concluded. P is equal to 0.18 and less than 1 which indicate $-1\ m/s^2$ is considered as insensitive to the flow.

**Table 4** Result Matrix of -1$m/s^2$ and the Flow

| Experimental results | | -1$m/s^2$ | | | | | Standard deviation of parameter influence |
|---|---|---|---|---|---|---|---|
| | | 50;50 | 100;100 | 150;150 | 200;200 | 250;250 | |
| Random seed | 10 | 1006 | 1014 | 1019 | 1018 | 1015 | 5.13 |
| | 20 | 1069 | 1069 | 1065 | 1066 | 1066 | 1.87 |
| | 40 | 1060 | 1059 | 1069 | 1066 | 1067 | 4.44 |
| | 80 | 1078 | 1084 | 1078 | 1077 | 1064 | 7.36 |
| | 160 | 1065 | 1057 | 1063 | 1059 | 1057 | 3.63 |
| Standard deviation of random seed | | 28.5 | 26.1 | 22.98 | 22.84 | 22.04 | |

### *5.4 Data Discussion*

According to all seventy-two result matrixes, the P value are collected and shown in Table 5. There is a one-to-one correlation between twelve simulation parameters from two core modules in VISSIM and six check indexes in the node (intersection) module, so there are seventy-two groups altogether.

**Table 5** Summary of P Values

| | Check index simulation parameter | flow | Average vehicle delay | Travel time | Number of stops | Maximum queue length | Average queue length |
|---|---|---|---|---|---|---|---|
| D | -1 | 0.18 | 0.29 | 0.31 | 0.48 | 0.5 | 0.6 |
| X2 | Multiple of the safety distance | 0.57 | 0.42 | 0.59 | *3.63 | **1.43 | 0.22 |
| X1 | Additional part of the safety distance | 0.31 | *3.54 | *3.67 | **1.18 | 0.39 | **1.41 |
| N | Number of vehicles observed | 0.15 | 0.64 | 0.74 | 0.48 | 0.74 | 0.26 |
| S | Safety distance conversion factor | *1.59 | **1.37 | 0.7 | 0.71 | 0.7 | 0.52 |
| C2 | Acceptable deceleration | 0.17 | 0.28 | 0.29 | 0.35 | 0.3 | 0.48 |
| R | Maximum deceleration of combined braking | 0.1 | 0.15 | 0.15 | 0.24 | 0.54 | 0.13 |
| A | Average parking distance | 0.77 | *4.35 | **1.45 | **1.32 | *1.83 | *1.57 |
| T | Waiting time before disappears | 0.03 | 0.1 | 0.03 | 0.17 | 0 | 0.12 |
| C1 | Maximum deceleration | 0.1 | 0.02 | 0.02 | 0.16 | 0.37 | 0.08 |
| O | Maximum forward distance | 0.31 | *1.73 | 0.74 | 0.74 | 0.7 | 0.41 |
| G | Minimum head space | 0.24 | 0.33 | 0.34 | 0.88 | 0.98 | 0.57 |

* P is greater than 1.5, ** P is between 1 and 1.5.

It can be concluded from Table 5:

(1) There are three sensitive simulation parameters to average vehicle delay: the additional part of the safety distance (P equals to 3.54), the average parking distance (P equals to 4.35), and the maximum forward distance (P equals to 1.73). And the P value of the safety distance conversion factor is 1.37, which is not so sensitive to the average vehicle delay;

(2) The statistical results show that average vehicle delay has three sensitive simulation parameters, which is the maximum among all check indexes. Secondly, the number of stops has one parameter that is sensitive to it, and two that are not so sensitive to it.

(3) The maximum queue length, the average queue length, and the travel time have two sensitive simulation parameters respectively, one is sensitive to it, and the other is not so sensitive.

(4) Safety distance conversion factor is the only.one sensitive parameters of the flow.

(5) The sensitivity between different check indexes and simulation parameters is different, and the number of sensitive parameters is different. Therefore, before the parameter calibration, it is feasible to use the sensitivity analysis method to

find the optimal check index, and to simplify the experimental steps and improve the simulation efficiency.

## Conclusions

In order to improve the accuracy and work efficiency, this paper proposed an optimized parameter calibration process, analyzed the parameter sensitivity of the model based on the variance analysis, and verified the correctness of the process with an actual example.

Five indexes in the node (intersection) module were selected as check indexes set. The basic parameters were used to construct a simulation model of signal intersection based on VISSIM. Selecting twelve simulation parameters in tow core module in VISSIM, the sensitivity analysis of simulation parameters of different check indexes was carried out, and the sensitive parameter sets of different check indexes are compared. Taking the intersection of Huangcun West Street and Xinghua Street in Daxing District of Beijing as an example, the sensitivity calculation method was designed, and the optimized process was verified.

The results show that:

(1) The average vehicle delay has maximum sensitive simulation parameters, followed by the maximum queue length, the average queue length and the travel time.

(2) A sensitivity analysis model based on variance analysis was established, and the basis for judging different sensitivities was given. The study found that the sensitivity of different check indexes to simulation parameters is different, and the number of sensitive parameters is different.

This paper proposed that the optimization process of the sensitivity analysis method to select optimal check index before the parameter calibration can streamline the experimental steps and improve the simulation efficiency.

**Acknowledgments:**This paper's fund number are ykj-2018-00597, 2018YFF0300305-07.

## References

[1] Li Yan. “Micro-simulation of roundabouts based on VISSIM.” Southwest Jiaotong University, 2014.
[2] Li Zhenlong, Wang Baoju, Jin Xue, and Lian Peikun. “Parameter calibration of VISSIM simulation models with a focus on main and side roads.” Journal of Transportation Information and Safety, 2015(2):45-50.
[3] Nurlan·Muhan. “Parameter calibration method of VISSIM model for road intersection based on self-adaptive orthogonal genetic algorithm.” Beijing Jiaotong University, 2014.
[4] Xu Yuexin, Wang Shuangshuang, Wu Hao. “Calibration of VISSIM lane change parameters based on uniform test method.” Journal of Shandong Jiaotong University, 2015, 23(3):5-8.
[5] Zhou Chenjing, Rong Jian, Chen Chun’an. “Parameter sensitivity analysis method for microscopic traffic simulation experiment.” Journal of Beijing University of Technology, 2016, 42(11):1728-1733.

# Jiangsu Easttrans Engineering Detection Co.,Ltd

As a leading comprehensive service provider in the field of detection and consulting, Jiangsu Easttrans Engineering Detection Co.,Ltd was invited to World Transport Convention(WTC) 2019 and shared the latest research results in new technology, new materials, new technique, highway engineering detection, informationization etc.

Wang Jie, chairman of the company, said' By innovating the detection technology, we can not only find out the problems immediately during the engineering construction process, but also make sure the good quality of the engineering, which is very important to the creation of quality engineering and the improvement of engineering quality. Detection should be objective, immediately, preventative, but it is too passive to find out the quality problem after the detection, thus we are always trying our best to transform from traditional detection to smart site management and control. We can find out the problems while the construction is going and solve the problems in time.'

In 2013,Easttrans first proposed 'Smart Site' in transport engineering construction field and constructed highway engineering construction quality control platform and APP based on internet of things, cloud computing, wireless sensing etc. which realized the collection, transmission, statistics, analysis, prevention, evaluation and assistant decision function of key parameters in highway construction process. It can also manage and control people, machine, material, method and environment in an all-round, real-time and effective way.

In the informationize construction aspect, Easttrans uses 3D mechanical control bulldozer, grader and unmanned road roller to realize the digital construction of subgrade. 3D mechanical control bulldozer and digital construction grader can realize the automatic leveling of subgrade filling without piling and lofting and can shorten the construction period. It can also control the thickness, gradient and smoothness accurately which maintain the elevation and horizontal error in ±2cm.The construction can be carried out 24 hours without interruption. The unmanned road roller can realize remote control and complete the basic motions like ignition, start, turning and braking. It can automatically enter the construction area, change paths and roll automatically according to the working environment on site and the preset construction parameters such as rolling trajectory, rolling speed, rolling times and vibration amplitude which avoids the leak and over rolling, overspeed and insufficient of rolling times caused by human factors.

Publisher: Viser Technology Pte. Ltd.

URL: www.viserdata.com

Add.:21 Woodlands Close, #08-18,
Primz Bizhub SINGAPORE (737854)